Author Manuscript

Author Manuscript

Author Manuscript

Author Manuscript

HHS Public Access

Author manuscript

Sci Signal. Author manuscript; available in PMC 2017 August 02.

Published in final edited form as:

Sci Signal. ; 9(439): ra77. doi:10.1126/scisignal.aae0546.

Peripheral motor neuropathy is associated with defective kinase regulation of the KCC3 cotransporter

Kristopher T. Kahle[1,*], **Bianca Flores**[2,*], **Diana Bharucha-Goebel**[3,4], **Jinwei Zhang**[1,5], **Sandra Donkervoort**[3], **Madhuri Hegde**[6], **Gulnaz Begum**[7,8], **Daniel Duran**[1], **Bo Liang**[9], **Dandan Sun**[7,8], **Carsten G. Bönnemann**[3,†,‡], and **Eric Delpire**[2,†,‡]

[1]Departments of Neurosurgery and Pediatrics and Cellular and Molecular Physiology, Centers for Mendelian Genomics, Yale School of Medicine, New Haven, CT 06510, USA [2]Department of Anesthesiology, Vanderbilt University School of Medicine, Nashville, TN 37232, USA [3]Neuromuscular and Neurogenetic Disorders of Childhood Section, Neurogenetics Branch, National Institute of Neurological Disorders and Stroke, Bethesda, MD 20814, USA [4]Department of Neurology, Children's National Health System, Washington, DC 20010, USA [5]MRC Protein Phosphorylation and Ubiquitylation Unit, College of Life Sciences, University of Dundee, Dundee DD1 5EH, Scotland [6]Department of Human Genetics, Emory University, Atlanta, GA 30322, USA [7]Department of Neurology, University of Pittsburgh, Pittsburgh, PA 15213, USA [8]Veterans Affairs Pittsburgh Health Care System, Geriatric Research, Educational and Clinical Center Pittsburgh, PA 15240, USA [9]Departments of Microbiology and Immunobiology, Harvard Medical School, Boston, MA 02114, USA

Abstract

Using exome sequencing, we identified a de novo mutation (c.2971 A>G; T991 A) in *SLC12A6*, the gene encoding the K^+-Cl^- cotransporter KCC3, in a patient with an early-onset, progressive, and severe peripheral neuropathy primarily affecting motor neurons. Normally, the WNK kinase—dependent phosphorylation of T^{991} tonically inhibits KCC3; however, cell swelling triggers Thr^{991} dephosphorylation to activate the transporter and restore cell volume. KCC3 T991A mutation in patient cells abolished Thr^{991} phosphorylation, resulted in constitutive KCC3 activity, and compromised cell volume homeostasis. $KCC3^{T991A/T991A}$ mutant mice exhibited constitutive KCC3 activity and recapitulated aspects of the clinical, electrophysiological, and histopathological findings of the patient. These results suggest that the function of the peripheral nervous system depends on finely tuned, kinase-regulated KCC3 activity and implicate abnormal cell volume homeostasis as a previously unreported mechanism of axonal degeneration.

‡Corresponding author. eric.delpire@vanderbilt.edu (E.D.); carsten. bonnemann@nih.gov (C.G.B.).
*These authors are co-first authors
†These authors are co-senior authors.

Author contributions: All authors contributed data to the manuscript. K.T.K., D.B.-G., S.D., J.Z., C.G.B., and E.D. wrote and revised the manuscript. All authors approved the final version.

Competing interests: The authors declare that they have no competing interests.

Data and materials availability: The KCC3-T991A mouse is available upon request.

Author Manuscript Author Manuscript Author Manuscript Author Manuscript

Introduction

Inherited peripheral neuropathies are heterogeneous, involving at least 75 different loci (1–3), and are classified in part, by whether the affected gene product involves the myelin sheath, axon, or both in sensory or motor neurons or both. Consideration of both the gene mutation and the resulting pathological and clinical phenotype is required to develop an appropriate diagnosis. This classification scheme is complicated however, because different mutations in the same gene can yield distinct disease phenotypes. For example, dominant gain-of-function (GOF) duplications in *PMP22*, encoding peripheral myelin protein 22, cause Charcot-Marie-Tooth disease 1A (CMT1A; OMIM #601097); in contrast, recessive loss-of-function (LOF) deletion in *PMP22* causes hereditary neuropathy with liability of pressure palsies (HNPP; OMIM #162500) (4). CMT1A is characterized by distal muscle weakness with atrophy, sensory loss, slowed nerve conduction velocity, and foot deformities. HNPP is a slowly progressing, pressure-induced demyelinating neuropathy causing mild symptoms, such as numbness and pain, to more severe symptoms involving muscle atrophy and paralysis of affected areas.

The SLC12A gene family encodes K^+-Cl^- cotransporters (KCCs), which are electroneutral transporters that use outwardly directed K gradients generated by the Na^+- and K^+-dependent adenosine triphosphatase (Na^+/K^+ ATPase) to mediate the regulated extrusion of K^+ and Cl^- ions from cells (5, 6). Hence, KCCs play important roles in cell volume homeostasis, epithelial transport, and neuronal excitability (7). KCC3 is encoded by SLC12A6, which is expressed in neurons and glial cells of the central nervous system (CNS) (8–10) and in the primary sensory (that is, the dorsal root ganglion) and motor nerves of the peripheral nervous system (PNS) (8, 11). The function and regulation of KCC3 in both the CNS and PNS are not well understood.

Autosomal recessive homozygous or compound heterozygous LOF mutations in *SLC12A6* cause the Mendelian disease agenesis of the corpus callosum with peripheral neuropathy (ACCPN; OMIM #218000) (9, 12, 13). ACCPN patients and KCC3 knockout (KO) mice exhibit severe peripheral nerve degeneration (11, 14–17); however, ACCPN patients also exhibit severe brain phenotypes, including mal-development of the corpus callosum, hydrocephalus, developmental delay, mental retardation, and seizures (14, 15). GOF mutations in KCC3 have not been identified in any organism, and the clinical consequences of overactive KCC3 in vivo are unknown.

Here, we describe a child with a severe and progressive peripheral neuropathy that affects primarily motor, rather than sensory, neurons and with normal brain structure and function. The patient harbored a de novo heterozygous mutation in KCC3 (T991A). Thr^{991} is an important regulatory site of KCC3 activity required for normal cell volume homeostasis, as demonstrated in human embryonic kidney (HEK) 293 cells (18–20). We show in patient-derived cells and in vivo with a mouse engineered with the same mutation that the T991A in KCC3 abolished WNK (with no lysine) kinase–dependent inhibitory phosphorylation of this site, thereby constitutively enhancing the activity of the transporter even under basal conditions. Dephosphorylation at this site normally occurs in response to cell swelling. These observations advance our understanding of KCC3 in human physiology, reveal a

Author Manuscript Author Manuscript Author Manuscript Author Manuscript

critical dependence of PNS neurons on kinase-regulated KCC3 activity, and implicate abnormal cell volume homeostasis as a previously unreported contributing mechanism to the pathogenesis of peripheral neuropathy.

Results

Clinical presentation of predominantly peripheral motor neuropathy

A 10-year-old boy presented to the Neuromuscular and Neurogenetic Disorders of Childhood Section at the National Institutes of Health (NIH) for diagnostic evaluation of an early-onset and progressive motor-predominant axonal neuropathy. At 9 months of age, the patient first exhibited foot dragging while cruising. At 15 months, he developed bilateral foot drop and experienced frequent falls when walking. He had no early delays in fine motor skill acquisition, but at 3 years of age, he had further progression, from distal to proximal, of leg weakness followed by hand weakness. At 8 years, he required an assistive device to ambulate. At 9 years, he lost the ability to independently ambulate. The patient reported no numbness, tingling, hearing problems, learning difficulty, or seizures. Cognitive development was normal as assessed by neuropsychological testing. Family history was noncontributory.

Upon examination at age 10 at the NIH, there were no dysmorphic features (such as high arched palate, abnormal distance between eyes, or syndactyly), and he had normal cognition, hearing, and language. There were no clinical signs of spasticity. He had pronounced muscle atrophy in his gastrocnemius, quadriceps, and hamstrings, as well as in his intrinsic hand muscles, biceps, and triceps. He had severe weakness in a distal to proximal distribution, with near lack of antigravity strength (scoring 2 of a possible 5) with attempted wrist extension and finger extension and spread, and scoring 1 to 2 of a possible 5 in strength in all lower extremity muscle groups. Deep tendon reflexes were absent. Vibration sense, joint position sense, and pinprick testing were normal.

At 6 years of age, nerve and muscle biopsies were performed at the Virginia Commonwealth University Children's Hospital. The nerve biopsy showed two nerve fascicles with mild loss of myelinated axons. A neurofilament stain also indicated mild axonal loss, whereas Luxol fast blue and Periodic acid–schiff stains indicated intact myelination. No onion bulbs were detected, indicating absence of demyelination followed by remyelination. Hematoxylin and eosin–stained sections of muscle showed scattered hypertrophic and numerous atrophic fibers, indicative of denervation. Adipose tissue and endomysial connective tissue were both increased in focal areas. Notably, there was no evidence of muscle regeneration or degeneration, inflammation (infiltration of immune cells), vasculitis (inflammation and narrowing of the blood vessels), or perifascicular atrophy (reduction in diameter of fibers in the periphery of the fascicle).

Brain magnetic resonance imaging (MRI) was unremarkable and revealed an intact corpus callosum, brain stem, cerebellum, and cortical folding pattern (Fig. 1, A and B). Comparison of muscle by ultrasound analysis between the patient and a healthy age- and gender-matched child revealed increased echogenicity (an indication of adipose or fibrous tissue), reduced bulk, and prominent atrophy (Fig. 1, C and D).

Author Manuscript Author Manuscript Author Manuscript Author Manuscript

Data from nerve conduction studies performed for the patient at age 7 and later at 9 years were compatible with the diagnosis of a progressive predominantly motor axonal neuropathy with secondary demyelinating features (Table 1). At 7 years of age, the tibial, median, and ulnar motor nerve studies all showed a marked reduction in amplitude with moderate slowing; the facial motor nerve was also reduced in amplitude. Median and ulnar sensory responses showed mildly reduced amplitudes with mild slowing; the sural sensory response was normal. At 9 years of age, the peroneal motor response was absent, and median and ulnar motor studies showed a further reduction in amplitude. The sural sensory response showed mild slowing, and the median and ulnar sensory responses showed a further mild reduction in amplitude and mild slowing of conduction velocity, indicating the presence of milder sensory nerve involvement in addition to the predominant motor neuropathy.

Blood counts were normal. The mean corpuscular volume and osmotic fragility of red blood cells were normal. Blood pressure and serum and urine electrolytes were normal (Table 2).

Identification of the mutation in the clinical case

Genetic testing before referral to our center included a negative complete CMT panel (including PMP22 deletion and duplication testing and sequencing, and *CX32, MPZ, PMP22, EGR2, NFL, PRX, GDAP1, LITAF, MFN2*, and SH3TC2 sequencing) and negative targeted sequencing for other relevant disease-causing genes, including *SETX, HSBP8, HSPB1, GARS, BSCL2, ATP7A, TRPV4*, and *IGHMBP2*. Clinical whole-exome sequencing of DNA derived from the blood of the patient and both of his parents was performed at the Emory Genetics Laboratory using the Agilent V5 Plus targeted sequence capture method and the Illumina HiSeq 2000 sequencing instruments. Variants were analyzed using bioinformatics analysis through the Emory Genetics Laboratory, with a “Neuropathy Boost option” to ensure complete coverage of genes known to cause neuropathy-related disease.

A heterozygous c.2971A>G (T991A) mutation in exon 22 of *SLC12A6*, the gene encoding KCC3, was identified (reference NM_133647.1) and confirmed by Sanger sequencing (Fig. 2A). Parental segregation testing was negative, demonstrating that the mutation was de novo. This mutation has not been previously reported in the literature and was not represented in any of the major databases of genetic mutations, including dbSNP, NHLBI EVS, ExAC Browser, or GEM (21). Thr^{991} is conserved among the four different human KCC family members (KCC1, KCC2, KCC3, and KCC4) and in KCCs across evolution (Fig. 2, B and C).

Thr^{991} resides in the KCC3 cytoplasmic C terminus and is a critical regulatory residue of transporter activity in response to cell swelling (22). To predict the effect of this mutation, we generated a structural model of the human KCC3 CTD (Fig. 2D), using the cytoplasmic domain of a prokaryotic cation chloride cotransporter (PDB ID: 3G40) as a template. Ala substitution at this site is predicted to have a functional impact by MutationTaster (23), SIFT (24), and PolyPhen-2 (25).

Author Manuscript Author Manuscript Author Manuscript Author Manuscript

Effect of KCC3 T991A mutation on KCC3 function

Given the importance of Thr^{991} phosphorylation in swelling-induced stimulation of KCC3 activity (18, 19), we assessed the phosphorylation and swelling-regulated function of KCC3 in patient and parental (control) fibroblasts. For positive controls, we expressed wild-type KCC3 or KCC3-T991A in HEK293 cells, which have low endogenous amounts of this protein (Fig. 3A). In all conditions tested, the T991A mutation significantly reduced KCC3 Thr^{991} phosphorylation, as assessed with a polyclonal phosphorylation-specific antibody that recognizes KCC3 when phosphorylated at this residue (19). The residual signal may represent incomplete absorption and removal of antibodies directed against the nonphosphorylated epitope.

The activity of KCCs, the Na^+-K^+-$2Cl^-$ cotransporters (NKCCs), and the Na^+-Cl^- cotransporters (NCCs) are regulated by a kinase cascade involving the WNK kinase family, which phosphorylates and activates the kinases SPAK and OSR1 (collectively referred to as SPAK/OSR1). Activated SPAK/OSR1 redundantly function to phosphorylate KCC, NKCC, and NCC proteins. WNK-dependent phosphorylation of KCCs inhibits their transporter function, whereas WNK-dependent phosphorylation of NKCCs stimulates their transporter function (26-28). Total abundance of KCC3, NKCC1, SPAK, OSR1, and extracellular signal-regulated kinase 1 (ERK1) signals appeared unchanged, whereas phosphorylated SPAK and NKCC1 signals increased upon exposure of the cells to the hypotonic low Cl^- solution (Fig. 3 A, bottom), confirming that the cells responded positively to this treatment, as described (19). Relative to parental fibroblasts, patient fibroblasts had ~50% less phosphorylation at Thr^{991} (Fig. 3, B and C), consistent with the heterozygous nature of the KCC3 T991A mutation. Phosphorylation at Thr^{1048} appeared unchanged (Fig. 3B).

To confirm that the mutation altered KCC3 function, we assessed K-Cl cotransport activity by measuring $^{86}Rb^+$ uptake under various conditions in HEK293 cells transfected with either wild-type or KCC3-T991A complementary DNA (Fig. 4A), or in human fibroblasts isolated from parental controls or the KCC3-T991A patient (Fig. 4B). Transporters and channels that can conduct K^+ can also conduct $^{86}Rb^+$, which is a radioactive ion that can be conveniently measured. To isolate the KCC-mediated flux, we exposed the cells to ouabain and bumetanide, which are inhibitors of the Na^+/K^+ pump and NKCC 1, the transporters that mediate the bulk (85%) of K^+ uptake in these cells (29), and then monitored Rb^+ uptake in the presence of hypotonic low-CF, conditions that cause an increase in cell volume and inactivation of the WNK-SPAK/OSR1 signaling pathway and increased KCC3 activity, and hypotonic low-K^+ conditions that also promote the cell swelling-induced dephosphorylation of Thr and Thr through activation of protein phosphatase-1 and protein phosphatase-2A (PP1/PP2A). We inhibited WNK-dependent SPAK/OSR1 activation with STOCK1S-50699, a drug that blocks the interaction between WNK and these downstream kinases and results in the activation of KCC3 by decreasing transporter phosphorylation, in part, at Thr (21, 22). Both untransfected and wild-type KCC3-transfected HEK293 cells showed a significant increase in K^+ influx upon WNK-SPAK OSR1 inhibition, consistent with increased KCC3 activity. In the absence of STOCK1S-50699, cells expressing KCC3-T991A exhibited significantly higher activity than cells expressing the wild-type KCC3. Furthermore, in all

Author Manuscript Author Manuscript Author Manuscript Author Manuscript

but the isotonic low-Cl^- control condition, WNK-SPAK/OSR1 inhibition produced no significant increase in K^+ influx, indicating no additional activation of the KCC3 (Fig. 4A).

To isolate KCC3 activity in the patient and parental fibroblasts, we measured K^+ influx in the presence and absence of furosemide, a KCC inhibitor (Fig. 4B). Both the parental and patient fibroblasts exhibited furosemide reduction in K^+ influx under all conditions tested (Fig. 4B). However, compared with the parental cells, fibroblasts isolated from the patient had a greater furosemide-sensitive K^+ flux (difference between flux measured in the absence and presence of furosemide) under hypotonic low-Cl^- conditions, indicating higher cotransporter activity in the patient cells compared with that in the parental cells (Fig. 4B). The KCC3-T991A fibroblasts have significantly higher K^+ flux compared with the parental control fibroblasts; furosemide-treated KCC3 control fibroblasts exhibit significantly decreased K^+ flux, and KCC3-T991A fibroblasts are also sensitive to furosemide treatment with significantly decreased K^+ flux.

We also assessed cell volume regulation in KCC3-T991A patient fibroblasts and parental control fibroblasts, using methods described previously (30). Parental cells exposed to hypotonic Hepes-MEM (150 mosmol/kg H_2O) exhibited a ~2.3 ± 0.6–fold increase in cell volume (at a rate of 1.03 ± 0.1% cell volume/min) (Fig. 4, C and D), which recovered to the original volume after returning cells to isotonic conditions. In contrast, the patient fibroblasts with KCC3-T991A had a compromised acute swelling response to hypotonic stress (1.4 ± 0.1-fold). These results are consistent with the hypothesis that the greater furosemide-sensitive flux in KCC3-T991A patient cells compromises cell volume regulation.

Generation and characterization of $KCC3^{T991A/+}$ and $KCC3^{T991A/T1991A}$ mice

Using CRISPR/cas9 gene editing, we created a mouse that reproduces the T991A mutation found in the human patient (Fig. 5, A to D). To demonstrate functional activation of K^+-Cl^- cotransport in this mouse, we isolated fibroblasts from mouse tails and measured K^+ influx through $^{86}Rb^+$ tracer uptake in the presence and absence of furosemide in an isotonic solution. As expected, under these conditions, the wild-type cells had very little K^+ flux, indicating very low KCC transporter activity (Fig. 5E). In contrast, we observed a high furosemide-sensitive K^+ influx in fibroblasts from KCC3-T991A heterozygous ($KCC3^{T991A/+}$) mice under these isotonic conditions, consistent with the mutation resulting in a constitutively active transporter (Fig. 5E).

We assessed motor function by accelerated rotarod test (31) in two cohorts of young [around postnatal day 40 (P40); mixed gender] mice with cohort 1 consisting of 12 wild-type and 12 KCC3-T991A heterozygous siblings $KCC3^{T991A/+}$, and cohort 2 consisting of 8 wild-type, 7 heterozygous $KCC3^{T991A/+}$, and 7 homozygous $KCC3^{T991A/T991A}$ siblings. In neither cohort of mice did the heterozygous mice exhibit impaired motor performance; however, homozygous mice ($KCC3^{T991A/T991A}$) exhibited a significant locomotor deficit (Fig. 5F).

To assess overall motor coordination and fine motor movements, we used the balance beam task (31). The mice first began their trials on the standard-sized square beam (12 mm). We found a significant difference in performance between wild-type mice and homozygous mice but no difference between heterozygous mice and wild-type mice (Table 3). During the task,

Author Manuscript Author Manuscript Author Manuscript Author Manuscript

wild-type and heterozygous mice quickly traversed the beam with little to no hindlimb paw slips, whereas the KCC3$^{T991A/T991A}$ mice displayed a tendency to stall, indicated by the delayed time to reach the platform, and experienced multiple hindlimb paw slips during their crossing (Table 3). To determine the robustness of this phenotype, we assessed the performance of the mice on a narrower 6-mm cross-sectional square beam. This size beam is considered a more difficult task for the mice, particularly for those that exhibit any limb deficits. On this beam, the wild-type and heterozygous mice continued to swiftly traverse with little to no paw slips (Table 3). However, the KCC3$^{T991A/T991A}$ mice experienced greater difficulty in crossing, with intense dragging of the hindlimbs and with multiple homozygous mice unable to complete the task. Three of the six homozygous mice began traversing the beam, displaying appropriate forelimb coordination, but would immediately fall due to the dragging of their hindlimbs and inability to properly place their hindlimbs onto the beam in coordination with the fore limbs. We scored the mice on beam walking by adapting the scoring method of Feeney *et al.* (32) to assign a neurological score to the mice: a score of 7 indicates that the mouse crossed the beam with no more than two paws and a score of 2 means that the mouse was unable to cross beam but maintained horizontal balance for at least 5 s (see Materials and Methods for details). Overall, we observed a significant effect of genotype on the beam walk score (Table 3). Whereas no significant differences were observed per trial within a genotype, there was a statistically significant difference between the beam walk performance of wild-type and T991A/T991A mice (Fig. 6A and Table 3).

We also tested for forelimb motor deficits with the wire hang grip test (31). We observed no significant difference between genotypes (Table 3). Whereas the mice were allowed to hang on the wire for 60 s, we observed the KCC3$^{T991A/T991A}$ mice clasping to the wire and thrashing to remain on the wire. They commonly used their hindlimbs and tail to secure themselves on the wire. Comparatively, both wild-type and KCC3$^{T991A/+}$ mice would often shift their grip to either side but mainly used their forelimbs. Thus, although the KCC3$^{T991A/T991A}$ mice demonstrated no statistical differences in their latency to hang on the wire, we observed a unique behavior that might indicate forelimb weakness. To further assess forelimb and hindlimb strength, we used the force grip assay, a noninvasive method that uses a bar attached to a force transducer. All of the mice were first weighed to account for variability in mass versus force (Table 3). We did not detect any significant differences in weight or grip strength among the three mouse genotypes (Fig. 6B and Table 3).

We next assessed nerve function on the basis of the amplitude of the compound muscle action potentials and the length of latencies using nerve conduction studies on the dorsal caudal tail nerve and the sciatic nerve (Fig. 6, C and D). The sciatic nerve and dorsal caudal tail nerve branch provide sensory and motor innervation to the upper and lower leg and tail, respectively. A decrease in amplitude is representative of axonal loss, and an increase in latency is representative of demyelination. We observed a trend toward a decreased amplitude for the sciatic nerve in heterozygous and homozygous mice compared with that of the wild-type mice, but the decrease did not reach statistical significance (Fig. 6D and Table 4). In contrast, we observed a significant reduction in the amplitude for motor function in the tail (Fig. 6C and Table 4). We also observed a statistically significant difference between wild-type and homozygous mice for the latencies in motor nerve tail conduction (Table 4).

Author Manuscript Author Manuscript Author Manuscript Author Manuscript

We also assessed sensory nerve function by increasing the gain to record smaller sensory signals. Amplitude and conduction latency measurements were made in all three genotypes. Sensory amplitudes were not statistically significantly different for either the tail or the sciatic nerve for sensory measurements (Fig. 6, C and D, and Table 4), but the sensory nerve latencies tended to be higher in the KCC3$^{T991A/T1991A}$ mice compared with the wild-type and KCC3$^{T991A/+}$ mice (Table 4). Traces recorded from the dorsal caudal nerve of wild-type and KCC3$^{T991A/T1991A}$ mice illustrate the differences in amplitude and response latency between genotypes (Fig. 6, E and F).

We assessed the integrity of sciatic nerves using ultrastructural analyses. Nerve fibers from wild-type and KCC3$^{T991A/T1991A}$ mice were cut transversally to observe the integrity of the myelin sheaths surrounding the axons (Fig. 7A). At high magnification (Fig. 7, B and C, for wild-type and Fig. 7, D and E, for homozygotes), there was no abnormal pathology. At lower magnification, both genotypes exhibited fibers with double rings of myelination (Fig. 7, F and G). These events are indicative of improper initial contact between axons and Schwann cells (33), which can occur under nonpathological conditions or may indicate a neuropathology. Upon closer examination, sections of the nerves from the KCC3$^{T991A/T1991A}$ mice also showed breakage of the myelin sheaths enwrapping the axon (Fig. 7, H and I). This degeneration seemed to be specific to the fibers showing double myelinating Schwann cells, suggesting that individual Schwann cells attempted remyelination but did not appear to succeed. This pathology was not observed in fibers that had a single, successful Schwan cell myelination. We quantified the occurrence of this double myelination breakage by counting the number of degenerating Schwann cells that was present in relation to normal single or double myelinating Schwann cells. In three homozygous sections, we observed 8 fibers with double-myelin breakages and 67 adjacent normal fibers, thus representing 10% of the total number. Comparatively, this was observed only once in over 50 sections of wild-type sciatic nerve.

Discussion

Our report presents the first human with a GOF mutation in KCC3, resulting from de novo substitution of Ala for Thr at amino acid position 991. This patient has an early-onset, severe, and progressive motor-predominant neuropathy. The regulated phosphorylation of Thr^{991} (in concert with Thr^{1048}) is a key mechanism controlling KCC3 activity in heterologous expression studies (18, 19). KCC3 is normally inactive in isotonic conditions due to inhibitory phosphorylation at Thr^{991} and Thr^{1048} (18, 19). Cell swelling causes rapid dephosphorylation of these sites by PP1 and PP2A to increase KCC3 activity (18, 19). When mutant KCC3 that cannot be phosphorylated at either Thr^{991} or Thr^{1048} due to alanine substitution is expressed in cultured cells, the mutant KCC3 exhibits constitutive activity (18, 19). Computer modeling predicted a close proximity of Thr^{991} to Thr^{1048} in KCC3 (Fig. 2D). Our patient's KCC3 T991A mutation recapitulates the constitutively active function found in KCC3 mutated and expressed in cultured cells. Furthermore, discovery of this mutation in human and reproducing the mutation in mouse provided a unique window to gain insight into the role of KCC3 function of the nervous system.

Author Manuscript Author Manuscript Author Manuscript Author Manuscript

Our combined clinical, genetic, neurobehavioral, and physiological results implicate this de novo GOF mutation in KCC3 as the cause of the patient's progressive motor-predominant neuropathy. We have not yet identified additional alleles with this mutation in the population, including patients suffering from peripheral nerve disease. On the basis of the known importance of Thr^{991} in the regulation of KCC3 activity and the data we presented, we propose that this heterozygous mutation causes the symptoms of the disease: (i) this mutation is de novo and extremely rare (that is, this variant is not present in the patient's parents or the general unaffected population, as expected for a dominantly acting pathogenic allele); (ii) Thr^{991} is conserved in all KCC family members across evolution; (iii) modeling programs predict high pathogenicity scores for T991A; (iv) reversible phosphorylation of Thr^{991} is a key mechanism limiting KCC3 activity and regulating cell volume homeostasis (18, 19); (v) KCC3 activity is high, and cell volume homeostasis is defective in the patient's fibroblasts, paralleling effects of this mutant protein expressed in HEK293 cells; and (vi) a homozygous mouse model of the T991A mutation exhibits motor nerve conduction and locomotor deficits. The importance of KCC3 in the nervous system is also supported by the abnormal, pathogenic central, and peripheral phenotypes associated with KCC3 LOF in both humans and mice (11, 12, 17).

Although our data with the $KCC3^{T991A/T991A}$ mice indicated that the pathology predominantly affected the hindquarters (tail and hindlimbs), we observed that homozygous mice required all four limbs with or without the tail to remain hanging on the wire. This indicates some forelimb weakness. In contrast to the human patient, we only observed locomotor deficits in the homozygous state in mice. Multiple precedents exist for dominant mutations causing human diseases, which can be only recapitulated in the homozygote state in the mouse. Such an example is lamin A (N195K), which in humans causes dilated cardiomyopathy with conduction system disease (34) in the heterozygous condition but in mice requires homozygous loss to be pathogenic (35). Differences between two species are not unexepected. Although there is overall conservation in proteins and function between mouse and human, the precise contribution of each protein to a function is likely to be species-specific because some factors in one species might better compensate for the loss of a protein than in the other species.

Our patient's clinical syndrome appears distinct from ACCPN, which features severe brain pathology and both sensory and motor peripheral neuropathies (nearly all ACCPN patients lack electrophysiological sensory responses and have only mildly reduced and slowed motor responses). ACCPN is due to recessive LOF KCC3 mutations commonly found in French Canadians (9, 12, 13, 36). In contrast, our patient has an early-onset and severe predominantly motor peripheral neuropathy, lacks clinical or radiographic brain pathology, and harbors a de novo GOF mutation in KCC3. Although the neurological and physiological examination of the patient indicated the neuropathy to be predominantly affecting motor nerves, evidence from nerve conduction studies showed that peripheral sensory nerves are also involved, albeit to a lesser extent. We also detected a trend toward decreased sensory function in the nerves of the $KCC3^{T991A/T991A}$ mice. ACCPN patients and KCC3 KO mice exhibit axonal swelling of spinal nerve roots and cranial nerves (9). This finding, our results with the T991A mutant patient and mice, along with the knowledge that Thr^{991} is dephosphorylated in response to cell swelling to trigger regulatory volume decrease,

Author Manuscript Author Manuscript Author Manuscript Author Manuscript

suggests that either excessive (for example, T991A GOF mutation) or insufficient KCC3 activity (for example, the LOF mutation that causes ACCPN)—dysregulated KCC3 activity—results in peripheral nerve dysfunction, although with somewhat different consequences (Fig. 8).

We show in human cells and in mice that KCC3 T991A abolishes the WNK1 kinase–dependent inhibitory phosphorylation at this site, resulting in a constitutively activated species of the transporter (Figs. 4 and 5). Dysregulation and constitutive transporter activation likely contribute to a failure of cell volume homeostasis in central or peripheral neurons with possible secondary axonal degeneration or loss. Consistent with this is the finding that KCC3-T991A patient cells exhibited significantly diminished cell swelling in response to acute hypotonic stress compared to the wild-type KCC3 parental cells. We propose that this molecular mechanism defines a novel form of CMT type 2. Phosphorylation-dependent regulation of KCC3 could also affect and thus alter neuronal excitability. In central neurons, control of intracellular Cl^- concentrations is mostly accomplished by the related transporter KCC2, which is restricted to the brain and spinal cord (37–41), but evidence exists for colocalization of KCC2 and KCC3 (8–10), possible heterodimerization (42), and their coregulation of neuronal $[Cl^-]_i$ (9). Whether the primary defect of the T991A mutation is dyregulation of cellular volume homeostasis or altered neuronal excitability due to altered intracellular Cl^- concentrations remains to be established.

The precise mechanism by which KCC3 affects peripheral nerve integrity is still unknown. Disruption in the transport properties of the cotransporter is certainly a reasonable explanation for the disorder, and data from various patients show that both LOF and GOF of KCC3 lead to peripheral nerve disease. At this point, however, we cannot dismiss the possibility that substitution of Thr^{991} into alanine leads to pathologies through mechanisms that are unrelated to the transport function of the cotransporter, although this seems very unlikely given the known role of this residue for transport function. For instance, membrane proteins are not present in isolation but interact with many other proteins, and disruption of the C terminus of KCC3 might affect one of these interactions. Similarly, the central versus peripheral origin of the disorder has yet to be settled. The neuropathy and locomotor phenotype observed in the global KCC3 KO mouse and ACCPN patients can be recapitulated by specifically knocking out KCC3 in neurons (17) and even more specifically by knocking out KCC3 in proprioceptive sensory neurons (16). Furthermore, severe pathology is observed in parvalbumin-positive sensory fibers in both global and parvalbumin-specific KCC3 KO mice. Thus, it is clear that KCC3 in sensory neurons is critical for PNS integrity. It remains to be tested whether a similar neuropathy and locomotor phenotype to observed in the various KCC3 KO mice can be elicited by knocking out KCC3 in motorneurons. If that is the case, we would conclude that both CNS and PNS neurons then contribute to the neuropathy. In the contrary, this would suggest that motor deficits observed in ACCPN patients and KCC3 KO mice are secondary to the sensory deficit.

It is also possible that loss of KCC3 function affects predominantly sensory neurons, whereas gain of KCC3 function affects mainly motor neurons. Because the PNS lacks KCC2, PNS neurons would be particularly dependent on KCC3. PNS neurons have a

Author Manuscript Author Manuscript Author Manuscript Author Manuscript

relatively higher resting concentration of intracellular Cl^- compared with CNS (43, 44). The presence of aquaporin water channels in PNS, but not in CNS, neurons may also make PNS neurons more dependent on the volume homeostatic function of KCC3 (22). In motor neurons, both KCC2 and KCC3 are present with KCC2 function predominant in lowering the intracellular Cl^- concentration (40, 45, 46). Constitutive or unregulated KCC3 activity in the motor neurons would likely upset the balance of KCC2 and KCC3 function, enhancing Cl^- extrusion and γ-aminobutyric acid (GABA)–mediated inhibition. Enhanced inhibition could negatively affect motor nerve conduction, because GABA inhibits motor neurons, thereby contributing to the neuropathy. Additional work will be required to fully establish all the neuronal cell types involved in the KCC3-mediated neuropathies.

Recognition of KCC3-mediated dysregulation as a disease mechanism identifies the transporter as a potential therapeutic target. KCC3, including the T991A mutant, is sensitive to inhibition by the loop diuretic furosemide, as we showed in our patient's fibroblasts. Identification of additional patients with activating KCC3 mutations may enable their treatment with clinically approved drugs. Dysfunctional kinase-mediated KCC3 regulation may also contribute to other forms of inherited or acquired neuropathies. For example, these findings may have relevance for diabetic peripheral neuropathy, a condition associated with accumulation of the intracellular organic osmolyte sorbitol (47), which is a sugar alcohol derived from fruit, corn, and other vegetables that is slowly metabolized in humans and is used as an artificial sweetener. Sorbitol is also an activator of WNK1 activity (48).

Materials and Methods

Patient recruitment

This study was approved by the Institutional Review Board of the National Institute of Neurological Disorders and Stroke (NINDS) and NIH. Written informed consent was obtained by a qualified investigator. DNA from blood and skin fibroblasts was obtained on the basis of standard procedures. Medical history was obtained, and clinical evaluations were performed as part of the standard neurologic evaluation.

Cell culture, transfections, and cell treatments

HEK293 and human fibroblast cells were cultured in 10-cm-diameter dishes in Dulbecco's modified Eagle's medium (DMEM) supplemented with 10% (v/v) fetal bovine serum, 2 mM L-glutamine, penicillin (100 U/ml), and streptomycin (0.1 mg/ml). For transfection experiments, each dish of adherent HEK293 cells was transfected with 20 μl of polyethylenimine (1 mg/ml; Poly-sciences) (49). Posttransfection cells (36 hours) were stimulated with either control isotonic or hypotonic medium for a period of 30 min. Cells were lysed in 0.3 ml of ice-cold lysis buffer/dish, lysates were clarified by centrifugation at 4°C for 15 min at 26,000*g*, and the supernatants were frozen in aliquots in liquid nitrogen and stored at −20°C. Protein concentrations were determined using the Bradford method. Where indicated, cells were treated with the indicated concentrations of the SPAK/OSR1 CCT domain inhibitor STOCK1S-50699 (50), which was purchased from InterBioScreen Ltd.

Author Manuscript Author Manuscript Author Manuscript Author Manuscript

Antibodies

We used antibodies recognizing the following proteins or phosphorylated sequences: KCC3 phospho-Thr^{991} [residues 975 to 989 of human KCC3 phosphorylated at Thr^{991}, SAYTYER(T)LMMEQRSRR]; KCC3 phospho-Thr$^{1039/1048}$ [residues 1032 to 1046 or 1041 to 1055 of human KCC3 phosphorylated at Thr$^{1039/1048}$, CYQEKVHM(T)WTKDKYM]; NKCC1 total antibody (residues 1 to 288 of human NKCC1); NKCC1 phospho-Thr^{203}/Thr^{207}/Thr^{212} antibody [residues 198 to 217 of human NKCC1 phosphorylated at Thr^{203}, Thr^{207}, and Thr^{212}, HYYYD(T)HTN(T)YYLR(T)FGHNT]; SPAK total antibody (full-length glutathione *S*-transferase–tagged human SPAK protein); SPAK/OSR1 (S motif) phospho-Ser^{373}/Ser^{325} antibody [residues 367 to 379 of human SPAK, RRVPGS(S)HLHKT, which is highly similar to residues 319 to 331 of human OSR1 in which the sequence is RRVPGS (S)GRLHKT]; OSR1 total antibody (residues 389 to 408 of human OSR1); and ERK1 total antibody (full-length human ERK1 protein). All antibodies were raised in sheep, affinity-purified on the appropriate antigen by the Division of Signal Transduction Therapy Unit at the University of Dundee, and previously characterized (19). Secondary antibodies coupled to horseradish peroxidase (HRP) used for immunoblotting were obtained from Pierce. Immunoglobulin G used in control immunoprecipitation experiments was affinity-purified from preimmune serum using Protein G Sepharose.

Buffers and solutions

Buffer A contained 50 mM tris-HCl (pH 7.5) and 0.1 mM EGTA. Lysis buffer contained 50 mM tris-HCl (pH 7.5), 1 mM EGTA, 1 mM EDTA, 50 mM sodium fluoride, 5 mM sodium pyrophosphate, 1 mM sodium orthovanadate, 1% (w/v) NP-40, 0.27 M sucrose, 0.1% (v/v) 2-mercaptoethanol, and protease inhibitors (1 tablet per 50 ml). Tris-buffered saline–Tween buffer (TTBS) contained tris-HCl (pH 7.5), 0.15 M NaCl, and 0.2% (v/v) Tween-20. SDS sample buffer was 1× NuPAGE LDS sample buffer (Invitrogen) containing 1% (v/v) 2-mercaptoethanol. Isotonic high-potassium buffer contained 95 mM NaCl, 50 mM KCl, 1 mM $CaCl_2$, 1 mM $MgCl_2$, 1 mM Na_2HPO_4, 1 mM Na_2SO_4, and 20 mM Hepes (pH 7.4). Hypotonic high-potassium buffer contained 80 mM KCl, 1 mM $CaCl_2$, 1 mM $MgCl_2$, 1 mM Na_2HPO_4, 1 mM Na_2SO_4, and 20 mM Hepes (pH 7.4). Isotonic buffer contained 135 mM NaCl, 5 mM KCl, 0.5 mM $CaCl_2$, 0.5 mM $MgCl_2$, 0.5 mM Na_2HPO_4, 0.5 mM Na_2SO_4, and 15 mM Hepes (pH 7.5). Hypotonic low-chloride buffer contained 67.5 mM sodium gluconate, 2.5 mM potassium gluconate, 0.25 mM $CaCl_2$, 0.25 mM $MgCl_2$, 0.5 mM Na_2HPO_4, 0.5 mM Na_2SO_4, and 7.5 mM Hepes (pH 7.5).

Immunoprecipitation with phosphorylation-specific antibodies

KCC3 phosphorylated at the Thr^{991} and Thr^{1048} residues was immunoprecipitated from human fibroblast cell lysates. The phosphorylation-specific antibody was coupled with Protein G Sepharose at a ratio of 1 mg of antibody/1 ml of beads. A total of 2 mg of clarified cellular lysates was incubated with 15 mg of antibody conjugated to 15 μl of Protein G Sepharose in the presence of lysate (20 μg/ml) of the corresponding nonphosphorylated peptide. Incubation was done for 2 hours at 4°C with gentle agitation, and the immunoprecipitates were washed three times with 1 ml of lysis buffer containing 0.15 M

Author Manuscript Author Manuscript Author Manuscript Author Manuscript

NaCl and twice with 1 ml of buffer A. Bound proteins were eluted with 1× LDS (lithium dodecyl sulfate) sample buffer.

Immunoblotting

Cell lysates (15 mg) in SDS sample buffer were subjected to electrophoresis on polyacrylamide gels and transferred to nitrocellulose membranes. The membranes were incubated for 30 min with TTBS containing 5% (w/v) skimmed milk. The membranes were then immunoblotted in 5% (w/v) skim milk in TTBS with the indicated primary antibodies overnight at 4°C. Sheep antibodies were used at a concentration of 1 to 2 mg/ml. The incubation with phosphorylation-specific sheep antibodies was performed with the addition of the nonphosphorylated peptide antigen (10 mg/ml) used to raise the antibody. The blots were then washed six times with TTBS and incubated for 1 hour at room temperature with secondary HRP-conjugated antibodies diluted 5000 fold in 5% (w/v) skimmed milk in TTBS. After repeating the washing steps, the signal was detected with the enhanced chemiluminescence reagent. Immunoblots were developed using a film automatic processor (SRX-101A, Konica Minolta Medical), and films were scanned with a 600–dpi (dots per inch) resolution on a scanner (Powerlook 1000, UMAX). Figures were generated using Photoshop/Illustrator (Adobe). The relative intensities of immunoblot bands were determined by densitometry with ImageJ software.

K^+ influx assay in human fibroblast cells and HEK293 cells

Human fibroblast cells were plated in 12-well plates (2.4-cm diameter per well), and the $^{86}Rb^+$ uptake assay was performed on cells that were 80% confluent. HEK293 cells were plated at a confluence of 50 to 60% in 12-well plates (2.4-cm diameter per well) and transfected with wild-type full-length KCC3 or a human disease mutant form of full-length flag-tagged KCC3 (T991A). Each well of HEK293 cells was transfected with 2.5 μl of polyethylenimine (1 mg/ml) and 1 mg of plasmid DNA. K^+ influx measurement, through $^{86}Rb^+$ uptake assay, was performed on the cells at 36 hours after transfection. In both cases, culture medium was removed from the wells and replaced with either isotonic or hypotonic medium for 15 min at 37°C. Cell medium was removed by means of aspiration with a vacuum pump and replaced with stimulating medium plus inhibitors including 1 mM ouabain and 0.1 mM bumetanide, to prevent $^{86}Rb^+$ uptake by the Na^+/K^+ AT Pase and NKCC1, for a further 15 min. After this period, the medium was removed and replaced with isotonic medium plus inhibitors containing $^{86}Rb^+$ (2 mCi/ml) for 10 min at 37°C. After this incubation period, cells were rapidly washed three times with the respective ice-cold nonradioactive medium. The cells were lysed in 300 μl of ice-cold lysis buffer, and $^{86}Rb^+$ uptake tracer activity was quantified with a PerkinElmer liquid scintillation analyzer. K^+ influx was calculated from $^{86}Rb^+$ uptake and expressed in picomoles K^+ per milligram of protein per minute.

CRISPR/cas9 generation of KCC3-T991A mice

A 20-bp sequence (ATATGAGCGCACCCTGATGA, boxed in Fig. 5A) located in exon 22 of mouse *Slc12a6* and followed by TGG as protospacer adjacent motif was selected for guide RNA targeting sequence. This sequence flanked by Bbs I sites was added to a guide RNA sequence in pX330, a vector expressing the guide RNA under a strong U6 promoter

Author Manuscript Author Manuscript Author Manuscript Author Manuscript

and cas9 under a hybrid chicken β-actin promoter. The vector was injected alongside a 179-bp repair oligonucleotide into 498 mouse embryos. The repair oligo contained 83-bp homology arms, a codon substituting Thr^{991} to Ala, a unique Sac I restriction site, and a few additional third base mutations to prevent targeting of cas9 to the repair DNA. Of 498 embryos injected, 283 were transferred to 13 pseudopregnant females, thereby generating 54 pups. At weaning, genotyping was done by amplifying a 479-bp fragment followed by Sac I digest. Eight Sac I–sensitive (positive) animals out of 54 (15%) were identified. We sequenced the Sac I–containing mutant alleles and identified four mice carrying the proper mutation, whereas the other four mice carried additional insertions or deletions (Fig. 5D). We selected two lines (#31 and #51) and crossed them to C57BL/6J mice to demonstrate germline transmission. The lines were then further bred to C57BL/6J to dilute any possible off-target effects.

Mouse fibroblasts

The tip of a mouse tail (5 mm) was minced using sterile fine forceps and sterile razor blades in a 35-mm culture dish containing 2 ml of DMEM/F12 containing penicillin (350 U/ml), streptomycin (350 mg/ml), and collagenase D (2 mg/ml) (from *Clostridium histolyticum*; Roche Diagnostics). The 2-ml medium containing small tail chunks was then added to 3 ml of identical medium in a 15-ml conical tube and rotated overnight at room temperature. The next day, 5 ml of complete DMEM/F12 medium [10% fetal bovine serum, penicillin (150 U/ml), and streptomycin (150 mg/ml)] was added to each tube, and the remaining large pieces of tails were allowed to sediment by gravity to the bottom of the tube (1 to 2 min). The supernatant (10 ml) was recovered, placed in new tubes, and spun at 150*g* for 4 min. The supernatants were aspirated, and the pellets were resuspended in 0.5-ml complete DMEM/F12 medium and placed in a 24-well plate for growth. Upon confluence, the cells were detached and successively moved to 35- and 100-mm plates.

$^{86}Rb^+$ uptake in mouse fibroblasts

Dishes (35 mm) were coated with 1 ml of water containing poly-D-lysine (0.1 mg/ml) overnight in a 37°C incubator. The dishes were then rinsed twice with 1 ml of water and covered with 2 ml of fibroblasts (1 × 10–cm dish resuspended in 16 ml of medium or 1:8 splitting ratio) for 2 hours of incubation at 37°C to allow the cells to stick. All dishes were plated from the same cell resuspension, thereby guaranteeing equal seeding. After 2 hours, the dishes were moved to room temperature and preincubated for 15 to 20 min in an isosmotic solution containing 140 mM NaCl, 5 mM KCl, 2 mM $CaCl_2$, 1 mM $MgSO_4$, 5 mM Hepes (pH 7.4), and 1 mM glucose. At the end of the preincubation period, the medium was aspirated and replaced with identical solution containing 100 mM ouabain, 20 mM bumetanide, and $^{86}Rb^+$ (1 mCi/ml) in the presence or absence of 2 mM furosemide. After the 15-min $^{86}Rb^+$ uptake, the dishes were washed three times with ice-cold buffer, exposed to 500 μl of 0.25 N NaOH for 1 hour, and neutralized with 250 μl of acetic acid glacial. Samples of 300 μl were added to 5 ml of scintillation fluid in glass vials for $^{86}Rb^+$ counts, and samples of 30 μl were used for protein assay (Bio-Rad). Each condition was done in triplicates, and K^+ flux was calculated from $^{86}Rb^+$ counts [counts per min (cpm)] and expressed in nanomoles K^+ per milligram of protein per minute. Calculation is based on measuring and averaging the counts (cpm) of 5 ml of aliquots of radioactive extracellular

Author Manuscript Author Manuscript Author Manuscript Author Manuscript

solution and relating these counts to the amount of K^+ contained in these aliquots (1 cpm = 2.5 pmol K^+).

Cell volume experiments

Cell volume changes in patient and parental cells were determined using calcein as a marker of intracellular water volume as described previously (20). Briefly, cells on coverslips were incubated with 0.5 mM calcein acetoxymethyl for 30 min at 37°C. The cells were placed in a heated (37°C) imaging chamber (Warner Instruments) on a Nikon Ti Eclipse inverted epifluorescence microscope equipped with perfect focus, a 40× Super Fluor oil immersion objective lens, and a Princeton Instruments MicroMAX CCD camera. Calcein fluorescence was monitored using a fluorescein isothiocyanate filter set (excitation, 480 nm; emission, 535 nm; Chroma Technology). Images were collected every 60 s with MetaFluor image acquisition software (Molecular Devices), and regions of interest (~10 to 15 cells) were selected. Baseline drift resulting from photobleaching and dye leakage was corrected as described previously (30). The fluorescence change was plotted as a function of the reciprocal of the relative osmotic pressure, and the resulting calibration curve was applied to all subsequent experiments as previously described (30). The Hepes-buffered isotonic solution contained (pH 7.4) 100 mM NaCl, 5.4 mM KCl, 1.3 mM $CaCl_2$, 0.8 mM $MgSO_4$, 20 mM Hepes, 5.5 mM glucose, 0.4 mM $NaHC0_3$, and 70 mM sucrose with 310 mosmol determined using an osmometer (Advanced Instruments). Anisosmotic solutions (150 and 280 mosmol) were prepared by removal or addition of sucrose to the above solution.

Accelerated rotarod assay

A neuromotor coordination task was performed using an accelerating rotating cylinder (model 47600; Ugo Basile, S.R. Biological Research Apparatus) in two cohorts of mice: 12 wild-type mice and 12 heterozygous T991A mice, and 8 wild-type, 7 heterozygous, and 7 homozygous mice. The cylinder was 3 cm in diameter and was covered with scored plastic. Mice were confined to a 4-cm-long section of the cylinder by gray Plexiglass dividers. Two to five mice were placed on the cylinder at once. The rotation rate of the cylinder increased over a 4-min period from 4 to 40 rpm. The latency of each mouse to fall off the rotating cylinder was automatically recorded by the device. Mice that remained on the rotarod during the 300-s trial period were removed and given a score of 300 s. The test was performed at three trials daily for three consecutive days with an intertrial interval of at least 30 min.

Wire hang grip test

To assess forelimb strength and coordination, we used the wire hang grip test. The wire was 50 cm long and 2 mm in diameter. The string was about 33.5 cm above the table surface with bedding placed underneath to prevent injury to any mice that fell. We trained the mice for two trials followed by three test trials in 1 day. The mice were allowed to hang on the wire for a maximum of 60 s, but timing ceased when the mouse fell. The mice were scored on latency to fall. Those that did not fall were given a score of 60 s.

Author Manuscript Author Manuscript Author Manuscript Author Manuscript

Force grip test

We used the Chatillon digital force meter (San Diego Instruments) to assess force grip strength in all limbs of the mice. Training and testing were done on the same day: we trained the mice for three practice trials with 10-min relief periods between each trial, followed by three test trials. The mice were allowed to initially grip the wire with all four paws and were then pulled horizontally with consistent force to determine grip strength. We normalized grip strength values to account for any variances due to body weight versus grip strength through the formula: $\text{Force}_{\text{mouse}}/\text{body weight}_{\text{mouse}}$.

Balance beam

To assess motor coordination and balance, we used a 1-m-long steel balance beam. We used two beams of varying thickness: a standard-sized beam (12 mm) and a thinner beam (6 mm), both of which had square cross sections to assess finer motor movements. The beam was placed about 50 cm from the ground and positioned between two pillars. At the start of the balance beam, mice began on an open, square platform and ended in an enclosed black box with bedding as motivation for the mice to cross. We trained the mice for 2 days (three trials per day for each beam) beginning with the thicker beam (12 mm) and progressing to the thinner beam (6 mm). The mice were tested consecutively on each beam with 10-min relief periods between each trial. The third day was used as a test day with three trials for each beam. The mice had about 60 s to traverse the beam and were scored on the neurological scoring system for beam walking adapted from Feeney and colleagues (32). This scoring system is based on the ability of the mouse to cross the beam and accounts for the number of paw slips. The mice received a score ranging from 1 to 7 based on their ability to complete the task, to place affected limbs on beam, and on the number of paw slips. This neurological scoring system considers a high score of 7 to be indicative of a wild-type mouse phenotype with no coordination deficits and a low score of 1 that is indicative of motor defects [score of 7, mouse crosses beam with no more than two paw slips; 6, can cross beam but uses affected limbs more than halfway along beam; 5, can cross beam but uses affected limbs less than halfway along beam; 4, crosses beam and can place affected limbs at least once on horizontal beam; 3, crosses beam but drags (affected) hindlimbs; 2, unable to cross the beam but can hold horizontal balance for at least 5 s; 1, unable to cross the beam].

Nerve conduction studies

We measured the nerve conduction amplitude and latency in both sensory and motor neurons of the mouse tail and the sciatic nerve. Mice were anesthetized with isoflurane vaporizer (Vaporizer Sales & Service Inc.) with a continual flow of oxygen. Body temperature was maintained with a warming pad. For tail nerve conduction studies, we determined tail motor latency through proximal stimulation using single Nicolet 0.4-mm steel needle electrodes (Rhytmlink International LLC) with an additional grounding electrode. For sensory and motor sciatic nerve measurements, we stimulated proximally the sciatic nerve. For all nerve conduction measurements, we stimulated at a duration of 20 ms and a stimulation range of 10 to 25 mA, with 25 mA being the supramaximal stimulus. We assessed latencies and traces using the Viking software, where latency is measured from initial onset to maximum negative peak.

Author Manuscript Author Manuscript Author Manuscript Author Manuscript

Transmission electron microscopy

Sciatic nerves were dissected from adult mice, then nerves were fixed with 2.5% glutaraldehyde in 0.1 M sodium cacodylate for 1 hour at room temperature (RT) and then at 4°C overnight. The Vanderbilt Electron Microscopy core further processed the sciatic nerves samples by washing them and fixing in 1% osmium tetroxide solution for 1 hour at RT and then with 0.5% osmium for 24 hours. The tissue samples underwent a series of ethanol dehydration steps (50% for 5 min, 75% for 15 min, 95% two times for 15 min, 100% three times for 20 min) before they were embedded in Spurr resin at 60°C for 24 to 48 hours. Semithin sections (500 nm) were stained with toluidine blue and examined for positioning. Ultrathin sections (80 nm) were then stained with uranyl acetate and lead citrate and placed on copper grids. Images were observed using a Philips/FEI T-12 transmission electron microscope.

Statistic analysis

Two-way ANOVA followed by Tukey's multiple comparisons test was used to assess statistical significance among wild-type, heterozygous, and homozygous groups of mice for the accelerated rotarod, wire hang grip, force grip, and balance beam behavioral assays, followed by Tukey's multiple comparisons test. For the force grip assay, we divided each force value obtained by the weight of the mouse ($\text{Force/mass}_{\text{mouse}}$) to account for any variation due to mass differences. For nerve conduction studies, we used one-way ANOVA followed by Tukey's multiple comparisons test to analyze statistical significance among all three genotypes. For all statistical analysis, we considered $P < 0.05$ to be statistically significant. GraphPad Prism (version 7.0, GraphPad Software Inc.) was used for all statistical tests.

Three-dimensional structure modeling

The three-dimensional structure of human KCC3 CTD was modeled by the I-TASSER server (51). Structure templates against the primary sequence KCC3 residues 733 to 1150 identified from the PDB database were used for comparative modeling. The top-ranking template is the cytoplasmic domain of a prokaryotic cation chloride cotransporter (PDB accession code 3G40), which shows 21.1% sequence identity with KCC3 CTD. Among the top five models predicted by I-TASSER, the one with good topology secondary structure assignment and a high C-score was chosen. The secondary structure elements of KCC3 were predicted by PredictProtein. PyMOL was used for molecular visualization.

Acknowledgments

We thank J. Skelton and L. Gower (Vanderbilt Transgenic Mouse/Embryonic Stem Cell Shared Resource) for their expertise in the injection and manipulation of mouse embryos. We also thank N. Byun (Department of Pharmacology, Vanderbilt University Medical Center) and A. Peltier (Department of Neurology, Vanderbilt University Medical Center) for their help in training and data analyses of nerve conduction experiments. We also thank D. R. Alessi (University of Dundee) for his support with the reagents and resources.

Funding: This work was supported by NIH research grant GM74771 (E.D.). K.T.K. was supported by a Harvard–Massachusetts Institute of Technology Neuroscience Grant, the Manton Center for Orphan Disease Research at Harvard Medical School, and the March of Dimes Basil O'Connor Award. C.G.B. is supported by intramural funds of the NINDS. B.F. and D.B.G. received support from NIH grants 2T32MH064913-11A1 and T32-AR056993, respectively.

Author Manuscript Author Manuscript Author Manuscript Author Manuscript

References and Notes

1. Tazir M, Hamadouche T, Nouioua S, Mathis S, Vallat JM. Hereditary motor and sensory neuropathies or Charcot–Marie–Tooth diseases: An update. J Neurol Sci. 2014; 347:14–22. [PubMed: 25454638]
2. Rossor AM, Evans MRB, Reilly MM. A practical approach to the genetic neuropathies. Pract Neurol. 2015; 15:187–198. [PubMed: 25898997]
3. Klein CJ, Duan X, Shy ME. Inherited neuropathies: Clinical overview and update. Muscle Nerve. 2013; 48:604–622. [PubMed: 23801417]
4. van Paassen BW, van der Kooi AJ, van Spaendonck-Zwarts KY, Verhamme C, Baas F, de Visser M. PMP22 related neuropathies: Charcot-Marie-Tooth disease type 1A and hereditary neuropathy with liability to pressure palsies. Orphanet J Rare Dis. 2014; 9:38. [PubMed: 24646194]
5. Lauf PK, Bauer J, Adragna NC, Fujise H, Zade-Oppen AMM, Ryu KH, Delpire E. Erythrocyte K-Cl cotransport: Properties and regulation. Am J Physiol. 1992; 263(Pt. 1):C917–C932. [PubMed: 1443104]
6. Adragna NC, Fulvio MD, Lauf PK. Regulation of K-Cl cotransport: From function to genes. J Membr Biol. 2004; 201:109–137. [PubMed: 15711773]
7. Gagnon KB, Delpire E. Physiology of SLC12 transporters: Lessons from inherited human genetic mutations and genetically engineered mouse knockouts. Am J Physiol Cell Physiol. 2013; 304:C693–C714. [PubMed: 23325410]
8. Pearson MM, Lu J, Mount DB, Delpire E. Localization of the K^+-Cl^- cotransporter, KCC3, in the central and peripheral nervous systems: Expression in choroid plexus, large neurons, and white matter tracts. Neuroscience. 2001; 103:481–491. [PubMed: 11246162]
9. Boettger T, Rust MB, Maier H, Seidenbecher T, Schweizer M, Keating DJ, Faulhaber J, Ehmke H, Pfeffer C, Scheel O, Lemcke B, Horst J, Leuwer R, Pape HC, Völkl H, Hübner CA, Jentsch TJ. Loss of K-Cl co-transporter KCC3 causes deafness, neurodegeneration and reduced seizure threshold. EMBO J. 2003; 22:5422–5434. [PubMed: 14532115]
10. Shekarabi M, Salin-Cantegrel A, Laganière J, Gaudet R, Dion P, Rouleau GA. Cellular expression of the K^+-Cl^- cotransporter KCC3 in the central nervous system of mouse. Brain Res. 2011; 1374:15–26. [PubMed: 21147077]
11. Byun N, Delpire E. Axonal and periaxonal swelling precede peripheral neurodegeneration in KCC3 knockout mice. Neurobiol Dis. 2007; 28:39–51. [PubMed: 17659877]
12. Howard HC, Mount DB, Rochefort D, Byun N, Dupré N, Lu J, Fan X, Song L, Rivière JB, Prévost C, Welch R, England R, Zhan FQ, Mercado A, Siesser WB, George AL Jr, Horst J, Simonati A, McDonald MP, Bouchard JP, Mathieu J, Delpire E, Rouleau GA. The K–Cl cotransporter KCC3 is a mutation in a severe peripheral neuropathy associated with agenesis of the corpus callosum. Nat Genet. 2002; 32:384–392. [PubMed: 12368912]
13. Uyanik G, Elcioglu N, Penzien J, Gross C, Yilmaz Y, Olmez A, Demir E, Wahl D, Scheglmann K, Winner B, Bogdahn U, Topaloglu H, Hehr U, Winkler J. Novel truncating and missense mutations of the KCC3 gene associated with Andermann syndrome. Neurology. 2006; 66:1044–1048. [PubMed: 16606917]
14. Labrisseau A, Vanasse M, Brochu P, Jasmin G. The Andermann syndrome: Agenesis of the corpus callosum associated with mental retardation and progressive sensorimotor neuronopathy. Can J Neurol Sci. 1984; 11:257–261. [PubMed: 6329500]
15. Deleu D, Bamanikar SA, Muirhead D, Louon A. Familial progressive sensorimotor neuropathy with agenesis of the corpus callosum (Andermann syndrome): A clinical, neuroradiological and histopathological study. Eur Neurol. 1997; 37:104–109. [PubMed: 9058066]
16. Ding J, Delpire E. Deletion of KCC3 in parvalbumin neurons leads to locomotor deficit in a conditional mouse model of peripheral neuropathy associated with agenesis of the corpus callosum. Behav Brain Res. 2014; 274:128–136. [PubMed: 25116249]
17. Shekarabi M, Moldrich RX, Rasheed S, Salin-Cantegrel A, Laganière J, Rochefort D, Hince P, Huot K, Gaudet R, Kurniawan N, Sotocinal SG, Ritchie J, Dion PA, Mogil JS, Richards LJ, Rouleau GA. Loss of neuronal potassium/chloride cotransporter 3 (KCC3) is responsible for the degenerative phenotype in a conditional mouse model of hereditary motor and sensory neuropathy

Author Manuscript Author Manuscript Author Manuscript Author Manuscript

associated with agenesis of the corpus callosum. J Neurosci. 2012; 32:3865–3876. [PubMed: 22423107]

18. Rinehart J, Maksimova YD, Tanis JE, Stone KL, Hodson CA, Zhang J, Risinger M, Pan W, Wu D, Colangelo CM, Forbush B, Joiner CH, Gulcicek EE, Gallagher PG, Lifton RP. Sites of regulated phosphorylation that control K-Cl cotransporter activity. Cell. 2009; 138:525–536. [PubMed: 19665974]
19. de Los Heros P, Alessi DR, Gourlay R, Campbell DG, Deak M, Macartney TJ, Kahle KT, Zhang J. The WNK-regulated SPAK/OSR1 kinases directly phosphorylate and inhibit the K^+–Cl^- co-transporters. Biochem J. 2014; 458:559–573. [PubMed: 24393035]
20. Adragna NC, Ravilla NB, Lauf PK, Begum G, Khanna AR, Sun D, Kahle KT. Regulated phosphorylation of the K-Cl cotransporter KCC3 is a molecular switch of intracellular potassium content and cell volume homeostasis. Front Cell Neurosci. 2015; 9:255. [PubMed: 26217182]
21. Gonzalez MA, Lebrigio RF, Van Booven D, Ulloa RH, Powell E, Speziani F, Tekin M, Schüle R, Züchner S. GEnomes Management Application (GEM.app): A new software tool for large-scale collaborative genome analysis. Hum Mutat. 2013; 34:842–846. [PubMed: 23463597]
22. Kahle KT, Khanna AR, Alper SL, Adragna NC, Lauf PK, Sun D, Delpire E. K-Cl cotransporters, cell volume homeostasis, and neurological disease. Trends Mol Med. 2015; 21:513–523. [PubMed: 26142773]
23. Schwarz JM, Rödelsperger C, Schuelke M, Seelow D. Mutation Taster evaluates disease-causing potential of sequence alterations. Nat Methods. 2010; 7:575–576. [PubMed: 20676075]
24. Ng PC, Henikoff S. SIFT: Predicting amino acid changes that affect protein function. Nucleic Acids Res. 2003; 31:3812–3814. [PubMed: 12824425]
25. Adzhubei IA, Schmidt S, Peshkin L, Ramensky VE, Gerasimova A, Bork P, Kondrashov AS, Sunyaev SR. A method and server for predicting damaging missense mutations. Nat Methods. 2010; 7:248–249. [PubMed: 20354512]
26. Kahle KT, Rinehart J, Lifton RP. Phosphoregulation of the Na–K–2Cl and K–Cl cotransporters by the WNK kinases. Biochim Biophys Acta. 2010; 1802:1150–1158. [PubMed: 20637866]
27. Gagnon KB, Delpire E. Molecular physiology of SPAK and OSR1: Two Ste20-related protein kinases regulating ion transport. Physiol Rev. 2012; 92:1577–1617. [PubMed: 23073627]
28. Alessi DR, Zhang J, Khanna A, Hochdörfer T, Shang Y, Kahle KT. The WNK-SPAK/OSR1 pathway: Master regulator of cation-chloride cotransporters. Sci Signal. 2014; 7:re3. [PubMed: 25028718]
29. Mathieu V, Chantôme A, Lefranc F, Cimmino A, Miklos W, Paulitschke V, Mohr T, Maddau L, Kornienko A, Berger W, Vandier C, Evidente A, Delpire E, Kiss R. Sphaeropsidin A shows promising activity against drug-resistant cancer cells by targeting regulatory volume increase. Cell Mol Life Sci. 2015; 72:3731–3746. [PubMed: 25868554]
30. Lenart B, Kintner DB, Shull GE, Sun D. Na-K-Cl cotransporter-mediated intra-cellular Na^+ accumulation affects Ca^{2+} signaling in astrocytes in an in vitro ischemic model. J Neurosci. 2004; 24:9585–9587. [PubMed: 15509746]
31. Karl T, Pabst R, von Hörsten S. Behavioral phenotyping of mice in pharmacological and toxicological research. Exp Toxicol Pathol. 2003; 55:69–83. [PubMed: 12940631]
32. Feeney DM, Gonzalez A, Law WA. Amphetamine, haloperidol, and experience interact to affect rate of recovery after motor cortex injury. Science. 1982; 217:855–857. [PubMed: 7100929]
33. Kidd GJ, Heath W. Myelin sheath survival following axonal degeneration in doubly myelinated nerve fibers. J Neurosci. 1991; 11:4003–4014. [PubMed: 1744700]
34. Fatkin D, Mac Rae C, Sasaki T, Wolff MR, Porcu M, Frenneaux M, Atherton J, Vidaillet HJ Jr, Spudich S, De Girolami U, Seidman JG, Seidman CE. Missense mutations in the rod domain of the lamin A/C gene as causes of dilated cardiomyopathy and conduction-system disease. N Engl J Med. 1999; 341:1715–1724. [PubMed: 10580070]
35. Mounkes LC, Kozlov SV, Rottman JN, Stewart CL. Expression of an LMNA-N195K variant of A-type lamins results in cardiac conduction defects and death in mice. Hum Mol Genet. 2005; 14:2167–2180. [PubMed: 15972724]
36. Salin-Cantegrel A, Rivière JB, Dupré N, Charron FM, Shekarabi M, Karéméra L, Gaspar C, Horst J, Tekin M, Deda G, Krause A, Lippert MM, Willemsen MA, Jarrar R, Lapointe JY, Rouleau GA.

Author Manuscript Author Manuscript Author Manuscript Author Manuscript

Distal truncation of KCC3 in non-French Canadian HMSN/ACC families. Neurology. 2007; 69:1350–1355. [PubMed: 17893295]

37. Blaesse P, Airaksinen MS, Rivera C, Kaila K. Cation-chloride cotransporters and neuronal function. Neuron. 2009:61, 820–838. [PubMed: 19840550]
38. Kaila K, Price TJ, Payne JA, Puskarjov M, Voipio J. Cation-chloride cotranspor-ters in neuronal development, plasticity and disease. Nat Rev Neurosci. 2014; 15:637–654. [PubMed: 25234263]
39. Kahle KT, Deeb TZ, Puskarjov M, Silayeva L, Liang B, Kaila K, Moss SJ. Modulation of neuronal activity by phosphorylation of the K–Cl cotransporter KCC2. Trends Neurosci. 2013; 36:726–737. [PubMed: 24139641]
40. Kahle KT, Delpire E. Kinase-KCC2 coupling: Cl^- rheostasis, disease susceptibility, therapeutic target. J Neurophysiol. 2016; 115:8–18. [PubMed: 26510764]
41. Kahle KT, Khanna AR, Duan J, Staley KJ, Delpire E, Poduri A. The KCC2 cotransporter and human epilepsy: Getting excited about inhibition. Neuroscientist. 2016:1073858416645087.
42. Ding J, Ponce-Coria J, Delpire E. A trafficking-deficient mutant of KCC3 reveals dominant-negative effects on K-Cl cotransport function. PLOS One. 2013; 8:e61112. [PubMed: 23593405]
43. Alvarez-Leefmans FJ, Gamiño SM, Giraldez F, Noguerón I. Intracellular chloride regulation in amphibian dorsal root ganglion neurons studied with ion-selective micro-electrodes. J Physiol. 1988; 406:225–246. [PubMed: 3254412]
44. Sung KW, Kirby M, McDonald MP, Lovinger DM, Delpire E. Abnormal $GABA_A$ receptor-mediated currents in dorsal root ganglion neurons isolated from Na–K–2Cl cotransporter null mice. J Neurosci. 2000; 20:7531–7538. [PubMed: 11027211]
45. Boulenguez P, Liabeuf S, Bos R, Bras H, Jean-Xavier C, Brocard C, Stil A, Darbon P, Cattaert D, Delpire E, Marsala M, Vinay L. Down-regulation of the potassium-chloride cotransporter KCC2 contributes to spasticity after spinal cord injury. Nat Med. 2010; 16:302–307. [PubMed: 20190766]
46. Stil A, Jean-Xavier C, Liabeuf S, Brocard C, Delpire E, Vinay L, Viemari JC. Contribution of the potassium–chloride co-transporter KCC2 to the modulation of lumbar spinal networks in mice. Eur J Neurosci. 2011; 33:1212–1222. [PubMed: 21255132]
47. Oates PJ. Polyol pathway and diabetic peripheral neuropathy. Int Rev Neurobiol. 2002; 50:325–392. [PubMed: 12198816]
48. Zagórska A, Pozo-Guisado E, Boudeau J, Vitari AC, Rafiqi FH, Thastrup J, Deak M, Campbell DG, Morrice NA, Prescott AR, Alessi DR. Regulation of activity and localization of the WNK1 protein kinase by hyperosmotic stress. J Cell Biol. 2007; 176:89–100. [PubMed: 17190791]
49. Durocher Y, Perret S, Kamen A. High-level and high-throughput recombinant protein production by transient transfection of suspension-growing human 293-EBNA1 cells. Nucleic Acids Res. 2002; 30:e9. [PubMed: 11788735]
50. Mori T, Kikuchi E, Watanabe Y, Fujii S, Ishigami-Yuasa M, Kagechika H, Sohara E, Rai T, Sasaki S, Uchida S. Chemical library screening for WNK signalling inhibitors using fluorescence correlation spectroscopy. Biochem J. 2013; 455:339–345. [PubMed: 23981180]
51. Yang J, Yan R, Roy A, Xu D, Poisson J, Zhang Y. The I-TASSER Suite: Protein structure and function prediction. Nat Methods. 2015; 12:7–8. [PubMed: 25549265]

Author Manuscript Author Manuscript Author Manuscript Author Manuscript

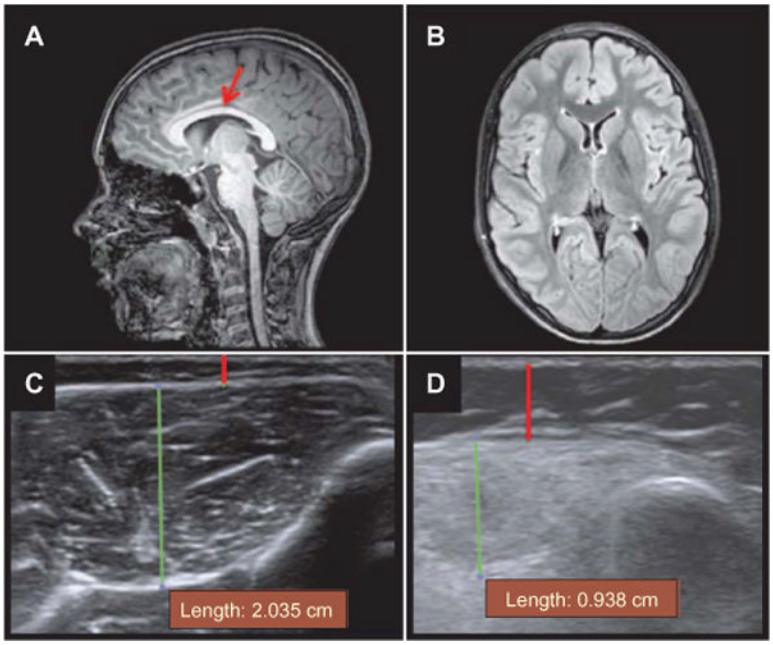

Fig. 1. Brain and muscle imaging of a patient with a KCC3 T991A mutation

(**A**) T1 sequence brain MRI, mid-sagittal view. Corpus callosum is indicated by red arrow. (**B**) Fluid-attenuated inversion recovery sequence brain MRI, axial view, demonstrating normal brain volume. (**C**) Muscle ultrasound (performed on Siemens Acuson S2000) of the tibialis anterior muscle from a healthy 10-year-old boy to represent normal echogenicity and bulk. (**D**) Abnormal muscle ultrasound of the tibialis anterior muscle from our 7-year-old patient. In (**C**) and (**D**), the green line indicates depth of muscle, and the red line indicates the subcutaneous fat layer.

Author Manuscript Author Manuscript Author Manuscript Author Manuscript

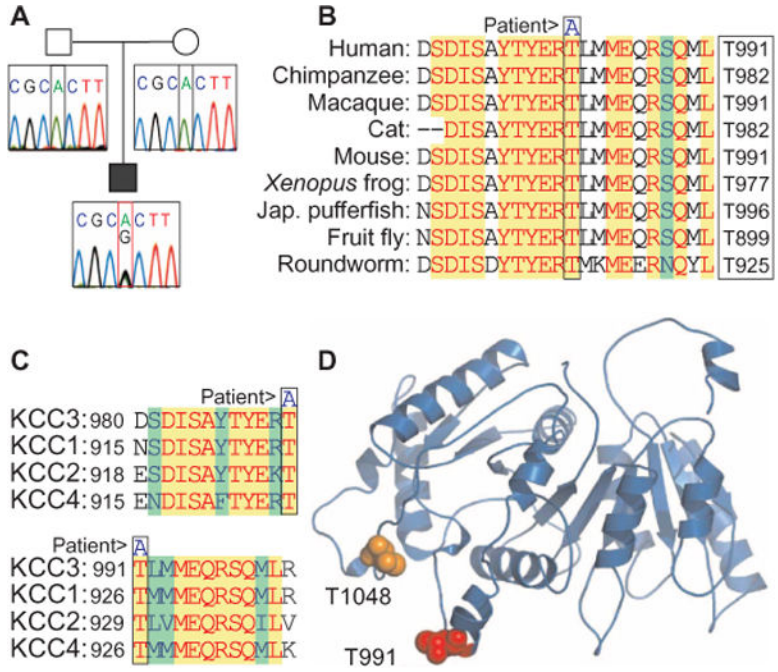

Fig. 2. Identification of a de novo KCC3 T991A mutation in a patient with an early-onset, progressive, and severe axonal motor neuron neuropathy

(A) DNA chromatograms illustrating the detection of a heterozygous c.2971A>G mutation in exon 22 of *SLC12A6*, encoding a T991A substitution in KCC3. (**B**) Evolutionary conservation of amino acid Thr^{991} in KCC3 across the indicated species. Jap, Japanese. (**C**) Conservation of the homologous residues of amino acid Thr^{991} in KCC3 in other human KCC family members. (**D**) Cartoon of the modeled structure of the human KCC3 C-terminal domain (CTD; residues 733 to 1150), based on homology modeling by I-TASSER using the prokaryotic cation Cl^- cotransporter [Protein Data Bank (PDB) ID: 3G40] as the template. Residues Thr^{991} and Thr^{1048} are presented in space fill and colored.

Author Manuscript Author Manuscript Author Manuscript Author Manuscript

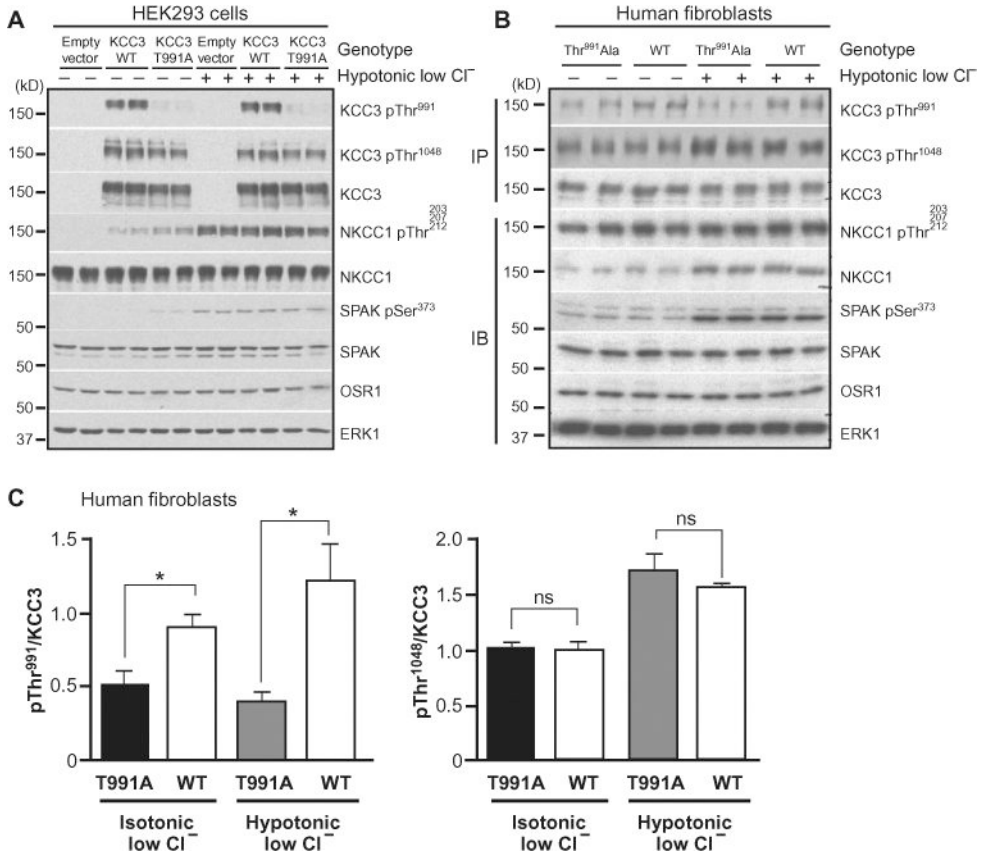

Fig. 3. T991A decreases KCC3 phosphorylation by the WNK1-SPAK pathway in HEK293 cells and patient fibroblasts

(A) Phosphorylation of wild-type KCC3 (WT) or KCC3 T991A expressed in HEK293 cells. HEK293 cells were transfected with the indicated constructs and exposed to hypotonic low-CP conditions for 30 min. Lysates were subjected to immunoblot (IB) with antibodies reocognizing the indicated proteins or phosphorylated proteins. ERK1 served as a loading control. (**B**) Phosphorylation of endogenous KCC3 and KCC3 T991A in human fibroblasts. Human fibroblast cells derived from the affected patient (heterozygous for KCC3 T991A) or his unaffected parental controls (WT) were exposed to hypotonic low-Cr conditions for 30 min. Lysates were subjected to immunoprecipitation (IP) with antibodies recognizing either KCC3 pThr991 or KCC3 pThr1048, and immunoprecipitates were immunoblotted with KCC3 total antibody. Lysates were also analyzed for the presence of the indicated proteins and phosphorylated proteins. (**C**) Quantification of the results of the Western blots shown in (B), statistically significant differences are indicated [repeated-measures one-way analysis of variance (ANOVA); $F(3, 4) = 14.54$, $P = 0.0129$]. Data are shown as means ± SEM. The quantification (ratio calculation) is based on phosphorylated species of KCC3/total KCC3. ns, not significant.

Author Manuscript Author Manuscript Author Manuscript Author Manuscript

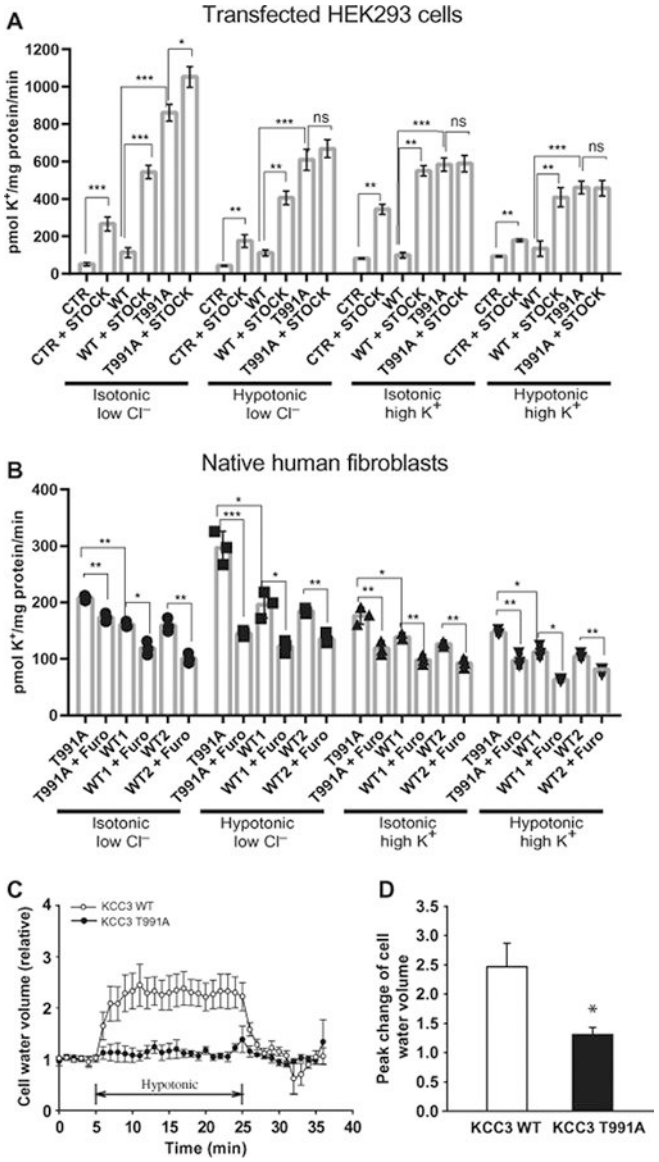

Fig. 4. T991A increases KCC3 activity and affects cell volume regulation in HEK293 cells and patient fibroblasts

(A) Transport activity of WT KCC3 and KCC3 T991A expressed in HEK293 cells. HEK293 cells were transfected and exposed to low-Cl^- in isotonic conditions (isotonic low Cl^-), hypotonic low-Cl^- conditions, high K^+ in isotonic conditions (isotonic high K^+), or hypotonic high-K^+ conditions in the presence or absence of STOCK1S-50699 (STOCK; WNK-SPAK/OSR1 inhibitor), for an additional 30 min in the presence of 1 mM ouabain (Na^+/K^+ ATPase inhibitor) and 0.1 mM bumetanide (NKCC1 inhibitor), to functionally isolate KCC activity. K^+ influx is presented in picomoles of K^+ per milligram of protein per minute and plotted for both isotonic and hypotonic conditions. K^+ uptake was significantly increased upon WNK/SPAK inhibition in untransfected and transfected cells [repeated-measures two-way ANOVA; $F(15, 40) = 38.43$, $P < 0.0001$]. KCC3-Thr^{991} Ala–transfected cells exhibited significantly higher activity than WT KCC3 in all conditions [$F(5, 40) = 813.9$, $P < 0.0001$]. (**B**) Activity of endogenous WT KCC3 (WT1 and WT2) and KCC3 T991A in human

Author Manuscript Author Manuscript Author Manuscript Author Manuscript

fibroblasts. Cells were exposed to the indicated conditions and then treated in the same conditions with 1 mM furosemide (Furo; a KCC inhibitor) for an additional 30 min in the presence of 1 mM ouabain and 0.1 mM bumetanide. K^+ influx was measured and analyzed as in (**A**). Data from a single representative experiment are shown as means ± SD. Statistical significance was determined by two-way ANOVA followed by Bonferroni post hoc tests (*P < 0.05, **P < 0.01, ***P < 0.001; ns, not significant or P > 0.05). Similar results were obtained in three separate experiments. (**C**) Relative change in cell water volume during acute hypotonic stress in KCC3 WT parental control fibroblasts and KCC3 T991A patient fibroblasts. Both cell types were exposed to isotonic Hepes–minimum essential medium (MEM) (310 mosmol/kg H_2O), followed by hypotonic Hepes-MEM (150 mosmol/kg H_2O) for 20 min, and then isotonic Hepes-MEM for 5 min. (**D**) Summary data of cell volume increase. KCC3 T991A patient cells exhibited abnormal regulatory volume decrease compared to KCC3 WT cells. Data are means ± SEM; n = 3 coverslips or experiments. *P = 0.02 versus WT.

Author Manuscript Author Manuscript Author Manuscript Author Manuscript

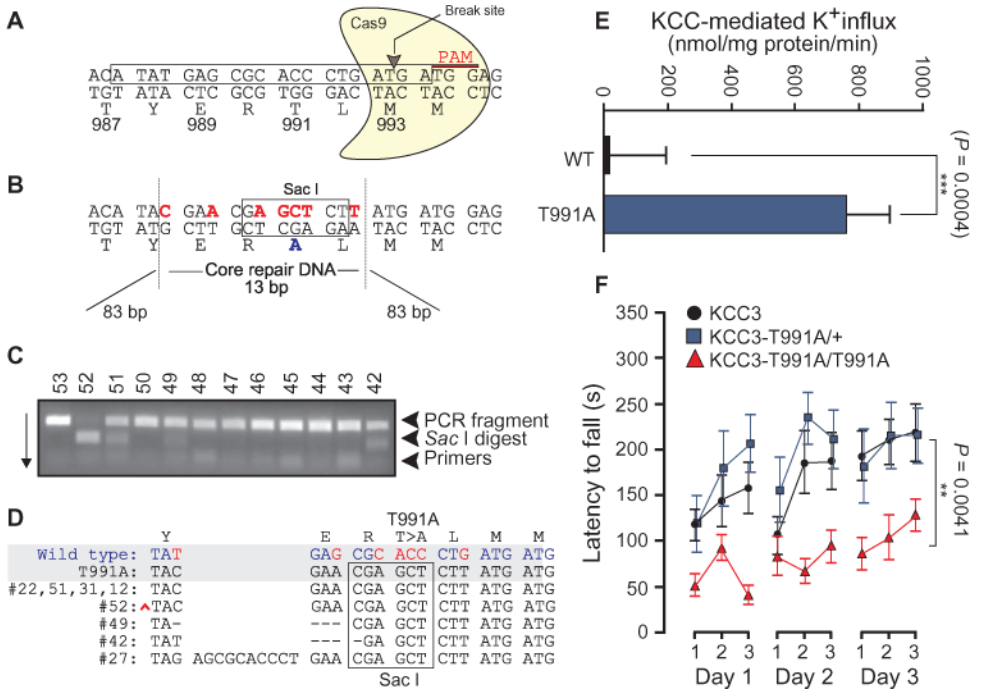

Fig. 5. Genetically modified KCC3-T991A mice exhibit locomotor deficits

(A) A portion of exon 22 of *Slc12a6* targeted for cas9 cleavage. A 20–base pair (bp) (boxed) target sequence, upstream of TGG as proto-spacer adjacent motif (PAM), was inserted into the guide RNA. **(B)** Schematic representation of a 179-bp repair fragment containing two 83-bp arms of recombination flanking a mutated 13-bp fragment. The codon change results in substitution of Thr^{991} into alanine and the introduction of a Sac I restriction site. (**C**) Sample genotyping gel showing a strong band (top) corresponding to full-length polymerase chain reaction (PCR) fragment. Arrow shows direction of band migration. Arrowheads indicate the presence of Sac I–digested bands. The PCR fragment in sample #52 is completely digested, indicating that the mouse is homozygous for the Sac I site. (**D**) Sequence of mutant alleles from eight Sac I–positive mice compared to the WT and intended mutant allele (shaded in gray). Four mice (#52, #49, #42, and #27) have additional base pair insertions or deletions. The ^ sign represents a 12-bp (TATGAGCGCACA) insertion upstream of the tyrosine codon. Only mice #22, #51, #31, and #12 had the desired mutation without other mutations. (**E**) K-Cl cotransport–mediated K^+ flux was measured under isosmotic conditions in fibroblasts isolated from WT and KCC3-T991A heterozygous mice (progeny of line #31). Flux was measured in triplicate under 0.1 mM ouabain, 20 μM bumetanide, and in the presence or absence of 2 mM furosemide. K-Cl cotransport is defined as the flux detected in the absence of furosemide minus the flux detected in the presence of furosemide. The experiment was reproduced once with similar data. (**F**) Accelerated rotarod data (seven to eight mice per group, age P40, and three trials a day for 3 days) report the time until the animal falls from the rod. KCC3-T991A WT, heterozygous, and homozygous mice were obtained from heterozygous breeding (line #31). Difference between genotypes was significant [two-way ANOVA; $F(2, 18) = 7.584$, $P = 0.0041$]. No difference was measured between WT and T991A/+ mice in the first cohort of 24 mice [two-way ANOVA; $F(1, 22) = 3.681$, $P = 0.0681$, or ns].

Author Manuscript Author Manuscript Author Manuscript Author Manuscript

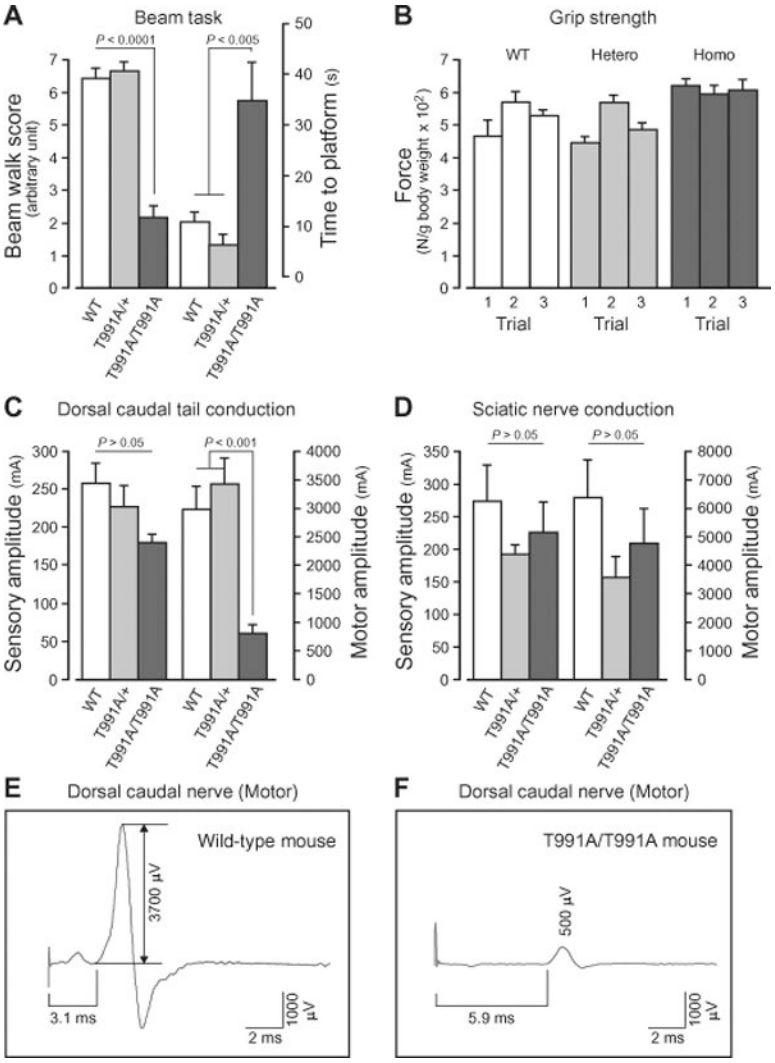

Fig. 6. Genetically modified KCC3-T991A mice exhibit hindlimb movement and nerve conduction deficits

(A) Response of WT, heterozygous (T991A/+), and homozygous (T991A/T991A) mice to the 6-mm-wide beam walk task. Mice were placed on the beam and allowed to cross to a safe platform. A performance score (1 to 7, see text) was given to each mouse (left axis). The time was also recorded (right axis). (**B**) Grip strength force was measured in all three genotypes using a bar attached to a force transducer. Data were corrected for body weight. The values (*y* axis) are in Newtons divided by gram of body weight. (**C**) Sensory (left axis) and motor (right axis) amplitudes of dorsal caudal tail nerve responses to 20 or 25 mA stimuli in WT, hetereozygous, and homozygous KCC3-T991A mice. (**D**) Sensory (left axis) and motor (right axis) amplitudes for sciatic nerves. Data were analyzed using one-way ANOVA followed by Tukey's post hoc tests; statistics are provided in Table 4. (E and F) Selected traces of motor conduction in dorsal caudal (tail) nerves from of WT and homozygous mice. The amplitude (in mV) is measured from the onset of the response peak to the top of the response peak. The latency to response is determined from the onset of the

Author Manuscript Author Manuscript Author Manuscript Author Manuscript

stimulus to the onset of the response peak. Tail nerves in this experiment were stimulated at 25 mA.

Author Manuscript Author Manuscript Author Manuscript Author Manuscript

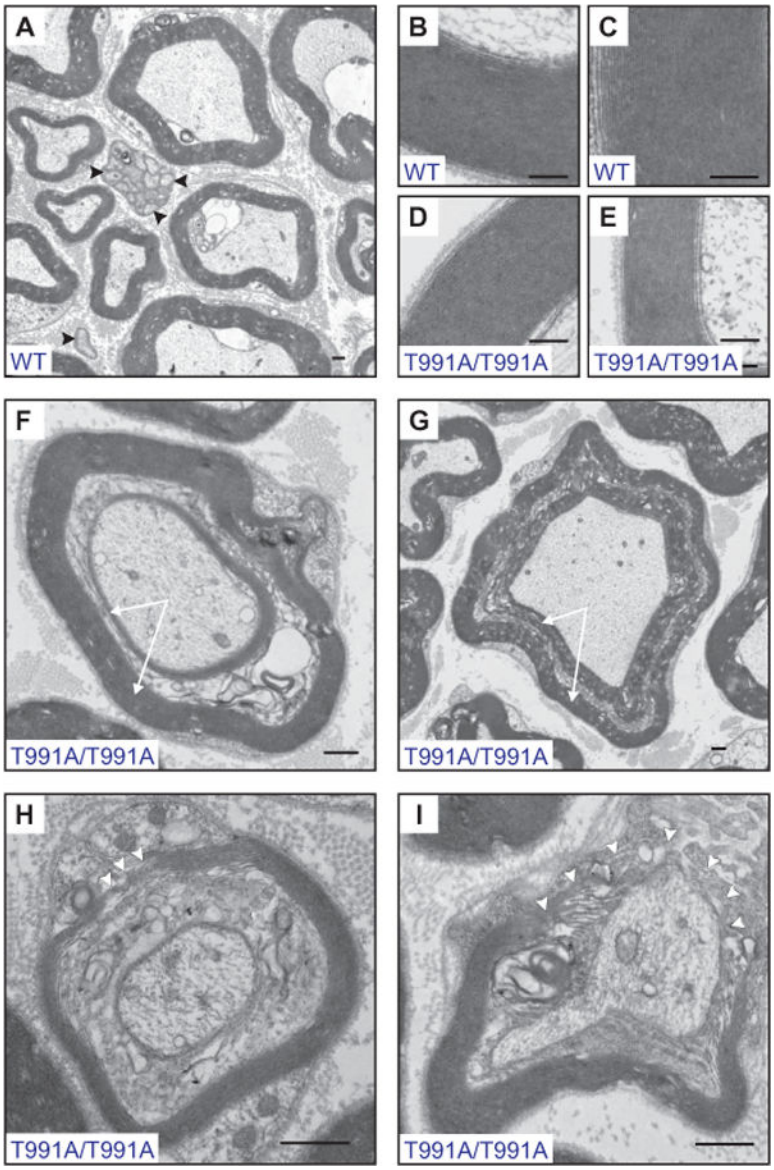

Fig. 7. Electron micrographs of sciatic nerve fibers isolated from KCC3 WT and T991A mice

Dissected fragments of sciatic nerves were fixed and processed for electron microscopy **(A)** Typical view of a transversally cut nerve fascicle (from WT mouse) showing most of the myelinated fibers and a few unmyelinated fibers (arrowheads). (B and C) Higher magnification of WT fibers showing packed myelin sheaths. (D and E) Similar views from homozygous T991A/T991A nerves. (F and G) Double myelination pathology observed in nerves from T991A/T991A mice. (H and I) Breakage in myelin observed in nerves from T991A/T991A mice. Scale bars, 500 nm.

Author Manuscript Author Manuscript Author Manuscript Author Manuscript

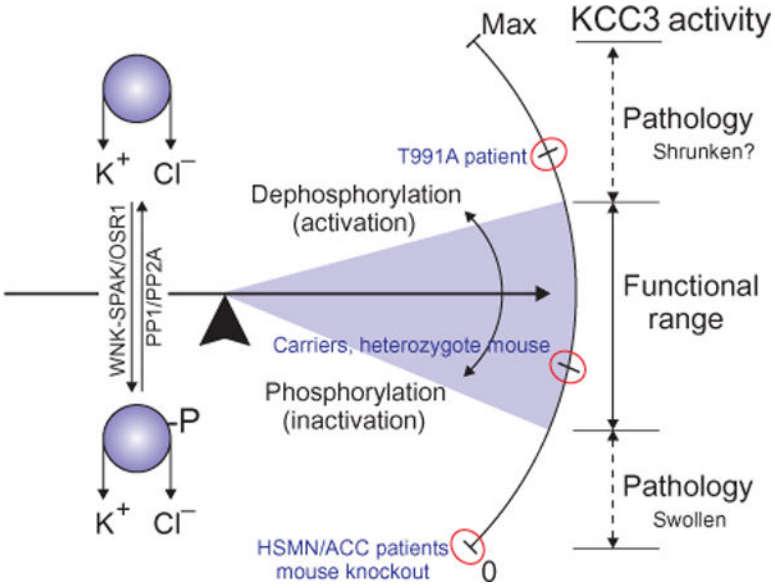

Fig. 8. Finely tuned KCC3 activity is required for structure and function of the human peripheral nervous system (PNS)

KCC3 activity, schematically represented on a scale from none (0) to maximal (max) activity, is contingent on the amount of KCC3 and a balance between the phosphorylated (inhibited) and dephosphorylated (activated) species of KCC3 in the neuronal plasma membrane. Insufficient KCC3 (for example, as occurs in ACCPN; OMIM #218000) due to LOF KCC3 mutations (or as seen in KCC3 KO mice) or excessive, unregulated KCC3 activity (asinthe patient described here withadenovo GOF KCC3 T991A mutation that abolishes a WNK1 kinase-dependent inhibitory phosphorylation event) results in severe and progressive peripheral axonal neuropathy with secondary demyelinating features, likely from impaired cell volume regulation and subsequent neurodegeneration. Normal humans and mice, as well as ACCPN carriers and KCC3 heterozygous KO mice, fall within a “functional range” that is free of significant pathology.

Author Manuscript Author Manuscript Author Manuscript Author Manuscript

Table 1

Nerve conduction studies with patient

Abnormal results are highlighted in bold. Amp, amplitude; DL, distal latency; CV, conduction velocity; LLN, lower limit of normal; ULN, upper limit of normal; N/A, not applicable; EDB, extensor digitorum brevis muscle (peroneal motor innervated muscle in foot); TA, tibialis anterior muscle (peroneal motor innervated muscle in leg); AHL, abductor hallucis longus muscle (tibialmotor innervated muscle in foot); ADM, abductor digitorum minimi (ulnar motor innervated muscle in hand); APB, abductor pollicis brevis (median motor innervated muscle in hand); NR, no response; NR^{A}, no response (no conduction velocity was calculated because the proximal site recording could not be elicited and a velocity could therefore not be calculated).

Nerve Motor nerve (and muscle)	7 years of age Amp (mV); (LLN)	9 years of age CV (m/s); (LLN)	DL (ms); (ULN)	Amp (mV); (LLN)	CV (m/s); (LLN)	DL (ms); (ULN)
Peroneal (EDB)	Not done	Not done	Not done	**NR**	**NR**	**NR**
Tibial (AHL)	**0.4** (>2.5)	**NR^{A}** (>40)	**6.1** (<6)	Not done	Not done	Not done
Median (APB)	**1.1** (>4.5)	**31** (>50)	**4.8** (<4.5)	**0.2** (>4.5)	**14** (>50)	**5.5** (<4.5)
Ulnar (ADM)	**0.5** (>4.5)	**14** (>50)	**4.3** (<3.5)	**0.1** (>4.5)	**NR**	**6.3** (<3.5)
Facial (nasalis)	**0.3** (>1.0)	N/A	**5.8** (<4.2)	Not done	Not done	Not done
Sensory nerve	**Amp (*m*V); (LLN)**	**CV (m/s); (LLN)**	—	Amp (mV); (LLN)	CV (m/s); (LLN)	—
Sural	17 (>6)	42 (>40)	—	8 (>6)	**27** (>40)	—
Median	**13** (>15)	**44 (>50)**	—	9 (>15)	**44** (>50)	—
Ulnar	7 (>15)	33 (>50)	—	6 (>15)	**41** (>50)	—

Author Manuscript

Author Manuscript

Author Manuscript

Author Manuscript

Table 2
Summary of clinical studies of a patient with a KCC3 T991A mutation

Test	Result
EMG *	Abnormal: Motor > sensory axonal neuropathy
MRI brain †	Normal
MR spectroscopy brain	Normal
Serum electrolytes ‡	Normal (except low creatinine)
Urine electrolytes §	Normal
Hearing	Normal in speech and pure tones and normal tympanometry and auditory brainstem response
Osmotic fragility	Normal erythrocyte osmotic fragility
Peripheral blood smear	No acanthocytes and normal smear
Creatine kinase	Normal (136)

* See Table 1 for specific nerve conduction study data and interpretation.

† See Fig. 1 for picture of normal MRI brain including normal brain volume and corpus callosum.

‡ Specific values are as follows: Na, 138; K, 3.9; Cl, 100; HCO_3^-, 23; Blood Urea Nitrogen (BUN), 9; and creatinine, 0.12 liters (normal, 0.3 to 0.7 liters).

§ Specific values are as follows: urine Na, 93; urine K, 86.5; and urine Cl, 124.

Author Manuscript Author Manuscript Author Manuscript Author Manuscript

Table 3

Size and strength properties of the engineered mice (second cohort). au, arbitrary units; WT, wild type.

Measure	Number of mice per genotype tested or experiments	WT	T991A/+	T991A/T991A	WT versus T991A/+(P)	WT versus T991A/T991A (P)	T991A/+ versus T991A/T991A (P)
Mass (g)	6, 7, and 6	27.1 ±1.9	31.3 ±1.6	22.7 ± .48	0.15	0.14	0.002
Rotarod	7, 7, and 7	169 ± 11	191 ±11	83 ± 6	0.73	0.02	0.0045
12-mm beam (time to cross the beam, s)	6, 7, and 6	6.3 ± 0.95	5 ± 0.3	16.38 ± 1.6	0.73	0.004	0.0005
12-mm beam (paw slips)	6, 7, and 6	0.05 ± 0.06	0.08 ± 0.06	9.9 ± 1.04	0.74	0.0001	0.0001
6-mm beam (failure to cross)	6, 7, and 6	1 of 6 mice in 1 of 3 trials	0	2 of 6 mice in 2 of 3 trials	N/A	N/A	N/A
6-mm beam	6, 7, and 6	6.4 ± 0.33	6.6 ± 0.21	2.1 ± 0.26	0.84	0.0001	0.0001
Grip test by wire	6, 7, and 6	27 ± 4.8	17.3 ± 3.2	38.8 ± 5.6	0.55	0.46	0.07
Force grip test (N/g)	6, 7, and 6	-0.045 ± 0.002	-0.041 ± 0.002	-0.051 ± 0.001	0.85	0.10	0.03

Sci Signal. Author manuscript; available in PMC 2017 August 02.

Author Manuscript Author Manuscript Author Manuscript Author Manuscript

Table 4

Nerve conduction measurements in engineered mice

Sensory and motor signals were measured in the dorsal caudal nerve (tail) and sciatic nerve (nerve) in WT, heterozygous (T991A/+), and homozygous (T991A/T991A) mice. Significance was tested by one-way ANOVA followed by Tukey's multiple comparison tests.

Measure	Nerve/signal	WT	T991A/+	T991A/T991A	Mice per genotype	WT versus T991A/+(P)	WT versus T991A/T991A (P)	T991A/+ versu T991A/T991A(P)
Amplitude	Caudal/sensory	265 ± 30	218 ± 61	213 ± 34	6, 6, and 6	0.73	0.68	0.99
	Sciatic/sensory	235 ± 78	192 ± 16	272 ± 77	5, 5, and 6	0.89	0.92	0.67
	Caudal/motor	2657 ± 634	2578 ± 770	943 ±215	5, 6, and 6	0.99	0.14	0.14
	Sciatic/motor	6521 ±1420	4223 ±1118	5393 ± 1661	6, 6, and 6	0.50	0.84	0.83
Latency	Caudal/sensory	1.58 ± 0.06	1.61 ± 0.04	1.70 ± 0.09	5, 6, and 6	0.95	0.38	0.51
	Sciatic/sensory	1.88 ± 0.33	1.71 ± 0.36	2.11 ± 0.15	5, 5, and 6	0.91	0.83	0.58
	Caudal/motor	3.20 ± 0.27	3.20 ± 0.53	4.80 ± 0.40	6, 6, and 6	0.99	0.03	0.03
	Sciatic/motor	2.74 ± 0.37	2.34 ± 0.11	3.50 ± 0.48	6, 6, and 6	0.72	0.32	0.09

Sci Signal. Author manuscript; available in PMC 2017 August 02.